

## Subsolidus phase relations in a mantle pyroxenite: an experimental study from 0.7 to 1.5 GPa --Manuscript Draft--

<b>Manuscript Number:</b>	ejm170130
<b>Article Type:</b>	Research paper
<b>Full Title:</b>	Subsolidus phase relations in a mantle pyroxenite: an experimental study from 0.7 to 1.5 GPa
<b>Short Title:</b>	Mantle pyroxenite subsolidus phase relations
<b>Abstract:</b>	<p>Pyroxenites are diffuse heterogeneity in the upper mantle and represent key lithologies in melting processes and mantle deformation. Mantle peridotites exposed in ultramafic massifs are often veined by pyroxenites. These latter experienced the same metamorphic evolution of host peridotite and may develop sensibly different phase assemblages in response to the different bulk composition. Despite of several experimental studies focused on melting relations in pyroxenites, subsolidus phase relations are still poorly known. We provide new experimental constraints on phase stability and mineral chemistry for a natural mantle pyroxenite. Piston cylinder experiments were conducted from 0.7 to 1.5 GPa, 1100-1250°C. Al-rich spinel, clinopyroxene, orthopyroxene and olivine are ubiquitous phases within the whole pressure range investigated. At 1100°C, plagioclase is stable up to 0.9 GPa; anorthite content [An = Ca/(Ca+Na)] decreases as a function of pressure from 0.70 at 0.7 GPa to 0.61 at 0.9 GPa. Maximum plagioclase modal abundance of 14 wt. % forms at 0.7 GPa; this amount is more than the double of that experimentally determined at same P-T in fertile lherzolite (5-6 wt. %). At intermediate pressure (1-1.4 GPa), modal spinel is almost constant (4-5 wt. %). A pyrope-rich garnet is stable at 1.5 GPa and its modal abundance increases with decreasing temperature from 5 to 10 wt. %, from 1230°C to 1150°C. Al content in pyroxenes varies significantly across the plagioclase-out and garnet-in transitions and is not pressure-dependent in the spinel pyroxenite field. At 1100°C, the plagioclase-out boundary occurs at comparable pressures in the pyroxenite and in fertile lherzolites. On the contrary, the garnet-in curve is located at significantly lower pressure than for mantle peridotites.</p>
<b>Keywords:</b>	Pyroxenites; experimental petrology; piston cylinder experiments; garnet stability; plagioclase; spinel; subsolidus assemblage; lithospheric mantle.

**Subsolidus phase relations in a mantle pyroxenite: an experimental study  
from 0.7 to 1.5 GPa**

Borghini, G. and Fumagalli, P.

*Dipartimento di Scienze della Terra, via Botticelli 23, 20133 Milano, Italy*

**Corresponding Author:**

**Giulio Borghini**

Dipartimento di Scienze della Terra « Ardito Desio »  
Università degli Studi di Milano  
Via Botticelli 23  
20133 Milano (Italy)

Email: [giulio.borghini@unimi.it](mailto:giulio.borghini@unimi.it)

**Keywords:**

Pyroxenites, experimental petrology, piston cylinder experiments, garnet stability, plagioclase,  
spinel, subsolidus assemblage, lithospheric mantle

## Abstract

Pyroxenites are diffuse heterogeneity in the upper mantle and represent key lithologies in melting processes and mantle deformation. Mantle peridotites exposed in ultramafic massifs are often veined by pyroxenites. These latter experienced the same metamorphic evolution of host peridotite and may develop ~~sensibly~~ different phase assemblages in response to the different bulk composition. Despite ~~of~~ several experimental studies focused on melting relations in pyroxenites, subsolidus phase relations are still poorly known. We provide new experimental constraints on phase stability and mineral chemistry for a natural mantle pyroxenite. Piston cylinder experiments were conducted from 0.7 to 1.5 GPa, 1100-1250°C. Al-rich spinel, clinopyroxene, orthopyroxene and olivine are ubiquitous phases within the whole pressure range investigated. At 1100°C, plagioclase is stable up to 0.9 GPa; anorthite content [ $An = Ca/(Ca+Na)$ ] decreases as a function of pressure from 0.70 at 0.7 GPa to 0.61 at 0.9 GPa. Maximum plagioclase modal abundance of 14 wt. % forms at 0.7 GPa; this amount is more than the double of that experimentally determined at same P-T in fertile lherzolite (5-6 wt. %). At intermediate pressure (1-1.4 GPa), modal spinel is almost constant (4-5 wt. %). A pyrope-rich garnet is stable at 1.5 GPa and its modal abundance increases with decreasing temperature from 5 to 10 wt. %, from 1230°C to 1150°C. Al content in pyroxenes varies significantly across the plagioclase-out and garnet-in transitions and is not pressure-dependent in the spinel pyroxenite field. At 1100°C, the plagioclase-out boundary occurs at comparable pressures in the pyroxenite and in fertile lherzolites. On the contrary, the garnet-in curve is located at significantly lower pressure than for mantle peridotites.

## 1. Introduction

Pyroxenites are considered a diffuse heterogeneity in the upper mantle (e.g. Bodinier & Godard, 2014). Despite they are volumetrically subordinated with respect to peridotites, pyroxenites play a key role in mantle melting processes (e.g. Hirschmann & Stolper, 1996; Phipps Morgan, 2001; Shorttle & McLennan, 2011; Lambart et al., 2016) and in mantle rheology (e.g. Hidas et al., 2013; Henry et al., 2017). Indeed, they have been invoked as diffuse components in mantle sources of basalts in several magmatic environments (e.g. Sobolev et al., 2005, 2007; Lambart et al., 2013 and references therein), and recognized as catalyst for lithosphere softening (Hidas et al., 2013).

Pyroxene-rich veins or layers embedded in mantle peridotites have been often observed in ophiolitic and orogenic ultramafic massifs (e.g. Bodinier & Godard, 2014 and references therein) and in mantle xenolithes (e.g. Gonzaga et al., 2010; Aulbach & Jacob, 2016) and their origin is usually related to high-pressure magmatic segregation, metamorphism and melt-rock reaction processes. Some of these pyroxenites represent long-lived deep mantle heterogeneity that experienced the same metamorphic evolution of the host peridotites at lithospheric mantle levels. However, pyroxenites are expected to develop sensibly different phase assemblages at fixed pressure (P) and temperature (T) conditions as a result of different bulk composition (e.g. Schmadicke, 2000). In particular, the P-T stability of aluminous phases is strongly affected by major elements composition, such as  $\text{Al}_2\text{O}_3$ ,  $\text{Cr}_2\text{O}_3$ , CaO and  $\text{Na}_2\text{O}$  contents. Experimental studies have suggested that, in pyroxenites garnet appears at significantly lower pressure than in peridotites (e.g. Irving, 1974, Adam et al., 1992), explaining the widespread occurrence of garnet-pyroxenites layers in spinel-bearing peridotites (e.g. Bodinier et al., 1987a and b; Garrido & Bodinier, 1999; Takazawa et al., 1999; Morishita & Arai, 2001; Montanini et al., 2006, 2012; van Acken et al., 2010; Gysi et al., 2011, Montanini & Tribuzio, 2015).


Although subsolidus phase relations in peridotites have been experimentally extensively investigated in both simplified and complex chemical systems (Fumagalli & Klemme, 2015 and references therein), very few experimental works have been focused on subsolidus phase equilibria in pyroxenites and the stability of aluminous phases is still only barely known (e.g. Irving, 1974; Adam et al., 1992).

In this paper we present and discuss the results of subsolidus experiments performed on a natural pyroxenite at pressure from 0.7 to 1.5 GPa and 1100-1230°C. Specific aim is to

investigate the stability of plagioclase, spinel and garnet in this peculiar pyroxenite bulk in order to provide useful geobarometric information for the subsolidus evolution of exhumed ultramafic mantle sectors.

## 2. Experimental and analytical methods

We selected ~~an olivine-websterite (pyroxenite GV10)~~, sampled in ophiolitic mantle sequences from External Liguride Unit (EL, Northern Apennines, Italy; Borghini et al., 2013, 2016) ~~and used as starting material~~. Pyroxenites from this mantle sector occur as cm-thick layers subparallel to the mantle foliation of host peridotite (Rampone et al., 1995; Borghini et al., 2013, 2016). Field, microstructural and geochemical observations indicated that they originated by pyroxenite melt-peridotite interactions, thus supporting its secondary origin (Lambart et al., 2012, 2013). Trace element compositions strongly suggest that many of these pyroxenite layers contained garnet in primary mineral assemblage, thus indicating crystallization at ~~rather~~ deep mantle level (Borghini et al., 2016). Much later ~~the~~ pyroxenite emplacement, inferred to ~~be~~ occurred at Ordovician ages (Borghini et al., 2013), this veined mantle sector experienced a subsolidus spinel- to plagioclase-facies decompressional tectonic evolution. This latter was associated to mantle exhumation during the extension of the Jurassic Tethys lithosphere and it is testified by plagioclase-bearing neoblastic assemblages in both peridotite and pyroxenite (Borghini et al., 2011, 2016).

The bulk composition of GV10  ~~reported in Table 1, together with other pyroxenite bulks~~ investigated in previous subsolidus experiments. Its melting relations at 1 and 1.5 GPa have been recently investigated (Borghini et al., 2017), and therefore the phase relations at solidus conditions are fully constrained.

Pyroxenite GV10 glass has been prepared from complete melting of rock powder in a gas mixing vertical furnace operating at FMQ  $fO_2$  and 1500°C at conditions and quenched in dry ice (Borghini et al., 2017). To promote the nucleation of the minor phases in subsolidus experiments, glass was seeded with 1% of a mixture of synthetic pure spinel (50%) and Dora-Maira pyrope (50%).

Experiments were performed at pressure from 0.7 to 1.5 GPa, and temperatures from 1100°C to 1250°C (Table 2), at the Laboratorio di Petrologia Sperimentale, Dipartimento di Scienze della Terra, University of Milano. Experiments up to 1.0 GPa were carried out in a

single-stage piston cylinder; for experiments at higher pressure an end-loaded piston cylinder was used. MgO-Pyrex-Salt assemblies have been adopted and run lasted from 94 to 495 hours (Table 2). Approximately 20 mg of starting material was loaded into a graphite inner capsule (outer diameter 2.8 mm), and then welded into an outer Pt capsule (outer diameter 3.0 mm, length about 7-8 mm). Graphite is used to isolate the sample from the Pt capsule and avoid Fe-loss (Kinzler, 1997; Walter, 1998). Furthermore, the graphite-Pt assembly keeps the oxygen fugacity below the graphite-C-O vapor buffer (Ulmer & Luth, 1991). In order to maintain anhydrous conditions, the platinum-graphite capsule with the starting material was dried in an oven at 250°C over a night before being rapidly welded shut. The thermocouple tip was separated from the platinum capsule by a 0.5-mm thick hard alumina disc. Assemblies were kept in oven at about 200°C for several hours before running the experiments. Temperature was measured by K-type and S-type thermocouples and is considered to be accurate to  $\pm 5^\circ\text{C}$ . An initial pressure of 0.25 GPa was applied, then the sample was first heated to 400°C for 10 minutes in order to soften the Pyrex, pressure was raised to the experimental value before reaching the desired temperature.

Capsules were enclosed in epoxy, sectioned lengthwise, polished and carbon-coated. Run products were inspected by back-scattered electron images (BSE) and microanalyses were performed using a JEOL JXA 8200 Superprobe equipped with five WDS-wavelength-dispersive spectrometers and one energy dispersive spectrometer (EDS) at the Dipartimento di Scienze della Terra, University of Milano. Both images and X-ray element maps were extremely useful in textural examination of the experimental charges. Analyses on mineral phases were performed using 1  $\mu\text{m}$  beam size and beam conditions of 15 kV and 5 nA. Counting time was 30 s for peak and 10 s for background.

### 3. Experimental results

#### 3.1. Textures and phase stability

Run products and experimental conditions are reported in Table 2 and summarized in Fig. 1. Textural observations show grain size varying between 2-25 $\mu\text{m}$  on average. As expected by the higher temperature, slightly coarser textures have been found in melt-bearing experiments (GV10-83-4 and GV10-83-16, Table 2).

A plagioclase-bearing assemblage composed of clinopyroxene, orthopyroxene, olivine, plagioclase and Cr-spinel is stable from 0.7 to 0.9 GPa at 1100°C. Pyroxenes form the larger grains (up to 25µm), usually showing euhedral prismatic habit (Fig. 2a). Olivine occurs as small sized crystals ( $\leq 5\mu\text{m}$ ), with a rounded habit (Fig. 2a). Plagioclase is homogeneously distributed in the run charges and occurs as subeuhedral crystals ranging in size from 2 to 8µm (Fig. 2a). Cr-bearing spinel forms thin rims on large relicts of spinel seeds, or occurs as small grains, around 2-3µm, homogeneously distributed within the charge (Fig. 2a). The extremely fine grain size of olivine and spinel in experiment at 0.7 GPa and 1100°C prevented to obtain satisfactory chemical analysis.

A spinel-bearing assemblage made by clinopyroxene, orthopyroxene, olivine and spinel is stable from 1 GPa at 1100-1180°C, to 1.4 GPa at 1150°C. In the experiments, clinopyroxene occurs as large grains of up to 20 µm showing triple joins (Fig. 2b). Orthopyroxene is easily recognizable in BSE images by its dark grey contrast and shows large prismatic habit (Fig. 2b). Rounded crystals of olivine up to 10µm in size have grey tone intermediate between clinopyroxene and orthopyroxene (Fig. 2b). Spinel is present as small rounded crystals up to 5µm in size.

A garnet-bearing assemblage composed of clinopyroxene, orthopyroxene, olivine, garnet and spinel is stable at 1.5 GPa and 1150-1230°C. These experiments are characterized by textures with grains size ranging between 2 and 10µm. Garnet is grown as rounded crystals either on or far from the garnet seeds (Fig. 2c), as revealed by Ca-Al X-ray mapping (Fig. 3). Rare spinel is present in garnet-bearing experiments as very small rounded grains (1-3µm), mostly recognized with the support of X-ray mapping (Fig. 3).

### 3.2. Minerals chemistry

Pyroxenes display significant chemical changes as a function of pressure. *Clinopyroxene* has  $X_{\text{Mg}}$  value [ $X_{\text{Mg}} = \text{Mg}/(\text{Mg}+\text{Fe}^{\text{tot}})$ ] between 0.83 and 0.85. In the garnet-bearing experiments ( $P > 1.4$  GPa), systematic higher  $X_{\text{Mg}}$  values reflect the coexistence with garnet having much lower  $X_{\text{Mg}}$ . The Al contents progressively increase with increasing pressure at 1100°C, in the plagioclase-bearing experiments and across the plagioclase-out curve (Fig. 4a). It ranges from 0.216 a.p.f.u. at 0.7 GPa, to 0.355 a.p.f.u. at 1.0 GPa, and is rather constant within the spinel facies (0.351-0.377) (Table 3). A slight Al decrease is also observed as garnet appears at 1.5 GPa, with Al content increasing from 1150 to 1230°C

(Table 3 and Fig. 4a). This is in agreement with results reported in experiments on peridotites in both CaO-MgO-Al<sub>2</sub>O<sub>3</sub>-SiO<sub>2</sub> system (Obata 1976; Herzberg, 1978; Gasparik, 1984) and more complex chemical systems (Borghini et al., 2010). Na content in clinopyroxene increases with pressure from 0.7 to 1.0 GPa at 1100°C, from 0.016 to 0.030 a.p.f.u., and varies 0.025-0.030 a.p.f.u. in spinel- and garnet-bearing experiments up to 1.5 GPa (Table 3). Ti contents are rather variable, ranging 0.009-0.015 a.p.f.u., without any dependence on pressure and temperature. Cr abundance is always lower than 0.006 a.p.f.u. (Table 3), reflecting the very low Cr content of the bulk (Table 1).

*Orthopyroxene* present X<sub>Mg</sub> values from 0.84 to 0.85, with only slight variations as observed in clinopyroxene. The Al content shows a positive correlation with pressure within the stability of plagioclase, increasing from 0.179 to 0.303 a.p.f.u. at 0.8 and 1 GPa respectively. It slightly decreases across the garnet-in curve at 1150°C (Table 4 and Fig. 4b). Ca contents vary between 0.049 and 0.071 a.p.f.u., and Ti abundance is as low as 0.003-0.007 a.p.f.u. (Table 4). As in clinopyroxene, Cr is very low (0.002-0.004 a.p.f.u.).

*Olivines* have homogeneous compositions with X<sub>Mg</sub> value [ $X_{Mg} = Mg/(Mg+Fe^{tot})$ ] around 0.83, and very low TiO<sub>2</sub> ( $\leq 0.03$  wt%) and Cr<sub>2</sub>O<sub>3</sub> ( $\leq 0.05$  wt%)(Table 5).

Reliable *spinel* compositions have been obtained mostly by combining WDS analysis with X-ray mapping on small rounded neoblasts isolated in the mineral matrix. In cases of very small grains, spinel compositions has been derived by removing the chemical effect of the contaminating host minerals, usually when spinel was included in clinopyroxene. All iron was considered as Fe<sup>2+</sup> and Fe<sup>3+</sup> was not calculated, because oxygen fugacity was not buffered. Spinel has X<sub>Mg</sub> values between 0.63 and 0.68 without any correlation with pressure and temperature (Table 6). Significant variations of X<sub>Cr</sub> are observed with the highest values in experiments within the plagioclase stability field, 0.079 at 0.8 GPa and 0.062 at 0.9 GPa (Table 6). On the contrary, X<sub>Cr</sub> value is very low in spinel-facies experiments, ranging 0.021-0.023 a.p.f.u., and increases in garnet-bearing experiments at 1.5 GPa. Furthermore a negative correlation with temperature from 1150 to 1230°C is also shown (Table 6). Ti content is usually lower than 0.006 a.p.f.u. (Table 6).

Despite its small grain size (usually < 10µm), we obtained several good *plagioclase* compositions with negligible contamination (MgO < 0.2 wt. %). Plagioclase is characterized by anorthite contents [ $An = Ca/(Ca+Na)$ ], which is negatively correlated with pressure (Table 7). At 1100°C, anorthite increases from 0.7 to 0.61 at pressure decreasing from 0.7 to 0.9 GPa, in excellent agreement with the An-pressure dependence documented by subsolidus experiments on lherzolite bulks (Fig. 5; Borghini et al., 2010, 2011; Fumagalli et al., 2017).

*Garnets* are pyrope-rich with  $X_{Mg}$  values of 0.75-0.76 and Ca content positively correlated with temperature ranging from 0.481 a.p.f.u. at 1150°C to 0.525 a.p.f.u. at 1230°C (Table 7).

### 3.3 Approach to equilibrium

Demonstration of equilibrium through reversal experiments is difficult in case of complex chemical systems and for continuous reactions. However, the approach to equilibrium is carefully assessed through the following observations: (1) the growth of compositionally homogeneous (Fig. 3), chemically unzoned minerals, likely enhanced by long-time duration of experimental runs (see Table 2), (2) systematic and consistent variations in mineral chemistry at different P-T conditions (Fig. 4 and 5), as well as coherent element partitioning, (3) maintenance of constant bulk composition, as supported by mass balance calculations (see below). Long duration of experiments led to the development of coherent textures with mineral phases homogeneously distributed in the charges. Furthermore, the behaviour of seeds can be taken into account to demonstrate a close approach to equilibrium; when not completely reabsorbed, seeds promoted growth rather than nucleation (Fig. 3).

## 4. Discussion

### 4.1. Mineral modal abundance and quantification of the reactions

Phase abundances have been derived by mass balance calculations using a weighted least-squares minimization procedure (Table 8). We included in the mass balance calculations eight major element oxides,  $SiO_2$ ,  $TiO_2$ ,  $Al_2O_3$ ,  $Cr_2O_3$ ,  $FeO$ ,  $MgO$ ,  $CaO$  and  $Na_2O$ . As the ferric/ferrous ratio is unknown in the run charges, all iron has been assumed as  $Fe^{2+}$ , although moderate  $Fe^{3+}$  amount can be contained in spinel. Representative results are shown in Figure 6, in which modal abundances (wt. %) are reported as a function of pressure at 1100 and 1150°C. Modal abundance of plagioclase decreases at increasing pressure until its breakdown at 1 GPa and this is accompanied by modal olivine decrease and spinel, pyroxenes increase. Quantification of the reaction governing the pressure-dependent plagioclase disappearance in

pyroxenite GV10 has been obtained by balancing mineral compositions across the plagioclase-out curve at 1100°C (Fig. 6), giving:

$$0.21\text{plag} + 0.21\text{ol} + 0.20\text{cpx}_1 + 0.35\text{opx}_1 + 0.03\text{sp}_1 = 0.42\text{cpx}_2 + 0.50\text{opx}_2 + 0.08\text{sp}_2. \quad (1)$$

This reaction is similar to that experimentally derived for mantle lherzolites (Borghini et al., 2010), but the higher plagioclase coefficient indicates that more modal plagioclase is involved in the pyroxenite, as expected by the higher bulk  $\text{Al}_2\text{O}_3$  and CaO contents. Plagioclase modal abundance of 14 wt. % forms at 0.7 GPa, 1100°C (Table 8); this amount is more than the double of that developed at same P-T in fertile lherzolite (5-6 wt. %, Borghini et al., 2010).

Additionally, relatively high bulk  $\text{Al}_2\text{O}_3$  in the pyroxenite results in modal spinel up to 4.7 wt. % (Table 8), almost twice than the spinel amount derived from experiments (2.5 wt. %, Borghini et al., 2010) and thermodynamic calculations (about 2.0 wt. %, Zibera et al., 2013) on fertile lherzolite bulks. Modal spinel is rather constant within the spinel-bearing experiments (4.1-4.7 wt. %), with no appreciable dependence on pressure (Fig. 5).

At  $P > 1.4$  GPa, 1150°C, the appearance of garnet is coupled with modal olivine increase and spinel, pyroxenes decrease, as documented at higher pressure in previous experimental works on ultramafic systems (e.g. O'Neill, 1981; Klemme & O'Neill, 2000; Walter et al., 2002; Klemme, 2004). Our mass balance calculations, accounting for mineral composition changes across the garnet-in curve at 1150°C (Fig. 6), yielded the following reaction:

$$0.04\text{sp}_3 + 0.38\text{cpx}_3 + 0.58\text{opx}_3 = 0.30\text{cpx}_4 + 0.51\text{opx}_4 + 0.17\text{gnt} + 0.02\text{ol} (+\text{sp}_4). \quad (2)$$

Cr-bearing rims on spinel seeds in garnet-bearing experiments have suggested that spinel is still stable at 1.5 GPa, together with garnet. However, quantification of  $\text{sp}_4$  in reaction (2) is made difficult by the high uncertainty on spinel composition due to its very small size. Reaction coefficient of  $\text{sp}_4$  obtained by balancing reaction (2) is well below 0.01 (around 0.002). Zibera et al. (2013) argued that very low spinel modes in many garnet peridotite xenoliths result in spinel overlooking. This effect is amplified in GV10 garnet pyroxenite having  $\text{Cr}_2\text{O}_3$  content ( $X_{\text{Cr}} = 0.01$ ) much lower than lherzolites ( $X_{\text{Cr}} = 0.07\text{-}0.10$ , Borghini et al., 2010).

#### 4.2. The effect of bulk pyroxenite composition on phase stability

Given the large compositional variability of pyroxenites, the bulk composition is relevant in depicting the phase assemblage stable at fixed pressure and temperature.

In peridotites the occurrence of garnet is related to the stability of the olivine-garnet join following the reaction spinel + pyroxenes = garnet + olivine (3) that defines the spinel to garnet facies transition (e.g. Kushiro & Yoder, 1966; O'Hara et al., 1971; Herzberg, 1978, Fumagalli and Klemme, 2015). It is well established that Cr strongly affects the location of spinel to garnet transition stabilizing spinel at higher pressure and resulting in spinel-garnet coexistence (Klemme, 2004). Similarly, the persistence of plagioclase to higher pressure has been established to be sensitive to the normative Ab/Di ratio and  $X_{Cr}$  of the bulk (Borghini et al., 2010).

In basalt-like compositions, the reaction plagioclase + pyroxenes + spinel = garnet (4) determines the lowest possible pressure whereby garnet is stable (e.g. Kushiro & Yoder, 1966; Herzberg, 1976). In this case a pyrope-grossular garnet appears at 1.3-1.5 GPa, 1000°C (Kushiro & Yoder, 1966). Variations in bulk  $X_{Mg}$  would however lead to the stability of an almandine-grossular garnet as breakdown product of olivine + plagioclase assemblages at much lower pressure, i.e. 0.7 GPa, 1000°C (Green and Hibberson, 1970).

The present study further shows the effect of bulk composition on the stable assemblage. Phase assemblages at 1 GPa, 1000-1100°C are plotted into the compositional space (Mg,Fe)O-CaO\*-SiO<sub>2</sub>-(Al,Cr)<sub>2</sub>O<sub>3</sub> for the system Cr-FNCMAS, constructed projecting mineral compositions from the exchange vectors CaAlNa-1Si-1, MgFe-1 and AlCr-1. The bulk compositions are indicated together with the value of normative plagioclase ( $Pl_{CIPW}$ ). GV10 presents the same phase assemblage, olivine, orthopyroxene, clinopyroxene and spinel of a fertile lherzolite (FLZ). The higher normative  $Pl_{CIPW}$  results in a higher modal abundance of clinopyroxene (and spinel) as the bulk approaches the orthopyroxene-clinopyroxene-spinel plane. At further increase of  $Pl_{CIPW}$  as observed in pyroxenite DR9734 ( $Pl_{CIPW} = 39.1$ ), the stable assemblage (orange star in Figure 7), at the same PT conditions is plagioclase, spinel clinopyroxene and garnet (Adam et al., 1992). It should be noted that the stable garnet in pyroxenite DR9734 has, as expected, slightly lower  $X_{Mg}$  (pyrope = 0.53 molar fraction) and higher Ca (grossular = 0.19) with respect to garnets stabilized in GV10 pyroxenite at higher pressure (at 1.5 GPa, 1150 °C, pyrope = 0.64, grossular = 0.14). Its occurrence is related to reaction (4).

In general, the clinopyroxene-orthopyroxene-spinel plane acts as a barrier separating olivine-bearing from olivine-free assemblages, the latter being able to stabilize associations of garnet and spinel, as observed in websterite R394 of Irving (1974), or garnet, spinel and plagioclase, as in clinopyroxenites DR9734 (Adam et al., 1992) and R392 (Irving, 1974).

In the following sections we will discuss plagioclase-out boundary, i.e. reaction (1) and garnet-in curve, i.e. reaction (2), as derived in the present experiments and in relation with peridotite bulk compositions.

#### 4.2.1 Near-solidus plagioclase-out curve

Defining the pressure limit of plagioclase stability in pyroxenites is useful to obtain information on geobarometric evolution of mantle rocks because pyroxenites are often associated to peridotites in ultramafic massifs.

Experimental studies in simplified chemical system CaO-MgO-Al<sub>2</sub>O<sub>3</sub>-SiO<sub>2</sub> (CMAS) have indicated that the stability of plagioclase lherzolite is limited at pressure below 1 GPa (e.g. Kushiro & Yoder, 1966; Obata, 1976; Gasparik, 1984). Subsolidus experiments on peridotite modeled in complex chemical systems revealed that the pressure of plagioclase-out curve is strongly influenced by the bulk Ab/Di ratio and X<sub>Cr</sub> (e.g. Green & Hibberson, 1970; Green & Falloon, 1998; Borghini et al., 2010). Higher bulk Ab/Di ratio leads to crystallization of a more albitic plagioclase, expanding the plagioclase stability towards higher pressure (e.g. Green & Hibberson, 1970; Walter & Presnall, 1994; Green & Falloon, 1998; Borghini et al., 2010; Fumagalli et al., 2017). Moreover, the plagioclase-out boundary is also sensitive to the bulk X<sub>Cr</sub> (or the chromite/anorthite normative ratio), which tends to stabilize the spinel rather than plagioclase (Borghini et al., 2010).

In [Figure 8](#) the plagioclase-out boundary derived for pyroxenite GV10 is compared with equilibria determined for different peridotite bulks. The high-pressure limit of plagioclase stability in GV10 occurs within the pressure range of the boundaries determined for lherzolites. In particular, at 1100°C the plagioclase-out curve of GV10 is very close to that of the Na-rich lherzolite HNa-FLZ recently studied by Fumagalli et al. (2017) ([Fig. 8](#)). This further supports that the effect of the much lower bulk X<sub>Cr</sub> of pyroxenite (0.01) is counterbalanced by its Ab/Di ratio (0.11) significantly lower than those of some mantle peridotites (Ab/Di = 0.15-0.30; Green & Falloon, 1998; Borghini et al., 2010).

As a result, plagioclase-facies recrystallization is expected to occur at very close

depths or, possibly, simultaneously in fertile lherzolites and in high-Mg pyroxenites, such as pyroxenite GV10 and R934 (Irving, 1974). This is consistent with the observations in ultramafic massifs where both pyroxenites and peridotites are partially re-equilibrated at plagioclase-facies conditions. This is the case of mantle sequences from EL ophiolites (Rampone et al., 1995; Montanini et al., 2006; Borghini et al., 2010, 2011, 2013, 2016), as well as, mantle tectonites in Ronda (e.g. Hidas et al., 2013). In agreement with experimental results, thermodynamically based estimates of plagioclase-facies recrystallization in Ronda mantle tectonites are within the pressure range of 1–0.5 GPa (Hidas et al., 2013).

Thermodynamic calculations of the plagioclase-out curve have been performed using the Perple\_X package (Connolly, 1990; Connolly & Petrini, 2002) in the chemical system Cr-NCFMAS, adopting the updated version of the Holland & Powell (1998) database and solid solution models for Cr-bearing pyroxenes, spinel and garnet (<http://www.perplex.ethz.ch>). At 1100°C, plagioclase-out curve computed by thermodynamic modeling is located at pressure of about 0.1 GPa lower than the experimentally-derived curve (Fig. 8). As discussed in Borghini et al. (2010), calculations result to be sensitive to the bulk Ab/Di ratio but do not consider the effect of bulk  $X_{Cr}$ . Pyroxenite GV10 has a very low  $X_{Cr}$  that is expected to move the plagioclase-out curve towards higher pressure (Borghini et al., 2010). On the contrary, computed curve is predicted at slightly lower pressure as effect of the low bulk Ab/Di (Table 1). Moreover, we found that the thermodynamic modeling overestimates the solubility of Al in pyroxenes, mostly in clinopyroxene (Fig. 4), and this also could contribute to reduce the field of plagioclase stability.

Results of this work suggest that, at 1100°C, anorthite content in plagioclase decreases with pressure, as observed in experiments on mantle peridotites (Fig. 5). In a recent paper, Fumagalli et al. (2017) proposed a geobarometer for plagioclase lherzolites based on the equilibrium  $\text{Fosterite} + \text{Anorthite} = \text{CaTschermak} + \text{Enstatite}$  (FACE geobarometer). Figure 5 shows that the relation between anorthite in plagioclase and  $X_{Al}^{M1}$  in clinopyroxene observed in experiments on GV10 pyroxenite is consistent with data on lherzolites. However, application of FACE geobarometer on experiments of the present study provides equilibrium pressures ( $0.65 \pm 0.05$ ,  $0.68 \pm 0.05$ ,  $0.75 \pm 0.05$  GPa) systematically lower than experimental pressures (0.7, 0.8, 0.9 GPa), with the highest deviation at the highest pressure. More experimental data on plagioclase-bearing pyroxenites are needed to extend the applicability of the FACE geobarometer to mafic compositions.

#### 4.3.3. Near-solidus garnet-in curve

The spinel- to garnet-facies transition is one of the major phase boundaries in the Earth's upper mantle and is relevant to investigate the chemical heterogeneity in the lithospheric mantle. A number of experimental studies have been dedicated to this transition in simplified chemical system, such as MAS and CMAS (for a review see Fumagalli & Klemme, 2015). In CMAS, the spinel-garnet boundary is univariant and, at near-solidus pressure, occurs at pressure 1.8-2.2 GPa (e.g. Milholland & Presnall, 1998; Klemme & O'Neill, 2000; Walter et al., 2002). Addition of Fe to the system tends to shift the garnet-in reaction towards lower pressure (O'Neill, 1981; Irifune et al., 1982; Webb & Wood, 1986; Nickel, 1986; Brey et al., 1999, Girnis et al., 2003) whereas the presence of Cr stabilizes spinel relative to garnet (e.g. Klemme, 2004). In particular, in Cr-bearing chemical systems spinel and garnet coexist until spinel breaks down, which is expected to occur at rather high pressure with depletion of peridotite (i.e. higher bulk  $X_{Cr}$ , Ziberna et al., 2013). Experimental studies on the stability of hydrated phases in peridotite complex system also documented the spinel-garnet transition at  $T < 1100^{\circ}C$  (e.g. Niida & Green, 1999; Fumagalli et al., 2005).

As discussed above, garnet-in curve for the GV10 pyroxenite is located just below 1.5 GPa, in agreement with the garnet appearance in pyroxenites with similar bulk composition (Fig. 7a), at lower pressure than garnet-in curves for all the peridotites (Fig. 9). However, experimental data in anhydrous peridotite system are scarce (Fumagalli & Klemme, 2015), making difficult the comparison with experiments on pyroxenites. Expansion of garnet stability toward lower pressure is promoted by higher FeO and  $Al_2O_3$  contents, as well as the lower  $X_{Cr}$  of the pyroxenites compared to the peridotites.

The garnet-in curve calculated by Perple\_X for the GV10 pyroxenite has a positive slope and, at near-solidus temperature of 1200-1330°C, is located about 0.4 GPa above the curve constrained by experiments (Fig. 9). As we discussed in the previous section, the modeling overestimates the Al solubility in pyroxenes and does not consider Ca in orthopyroxene (Fig. 4). Calculations also tend to underestimate Cr solubility in pyroxenes, as previously documented applying the same thermodynamic calculation on various lherzolites (Ziberna et al. 2013, Borghini et al., 2010, Fumagalli et al., 2017). As a consequence, spinel composition derived by thermodynamic modeling is much Cr-richer than the spinel observed in experiments. This could increase the predicted stability of the spinel over garnet and plagioclase, expanding the field of spinel-facies in Mg-rich pyroxenites, as well as in peridotites, both toward higher and lower pressure (Fig. 8 and 9).

## 5. Concluding remarks

1) We have experimentally investigated the subsolidus phase relations in secondary-type pyroxenite GV10 from 0.7 to 1.5 GPa, 1100-1230°C. Spinel, olivine and pyroxene are stable within the whole pressure range studied here. Plagioclase is observed from 0.7 to 0.9 GPa and garnet occurs solely at 1.5 GPa.

2) Plagioclase composition is influenced by pressure, with anorthite decreasing from  $An = Ca/(Ca+Na) = 0.70$  at 0.7 GPa to  $An = 0.61$  at 0.9 GPa. At 0.7 GPa (1100°C), modal plagioclase produced in the studied pyroxenite by metamorphic reaction is more than twice that found in fertile lherzolites. Spinel modal abundance increases at decreasing pressure in plagioclase-bearing experiments and at decreasing temperature where it coexists with spinel at 1.5 GPa. Garnet has pyrope-rich compositions and its modal abundance increases with decreasing temperature up to 10 wt. %, at 1150°C.

3) Pyroxenites having bulk composition characterized by high  $X_{Mg}$  and relatively low normative Plagioclase ( $Pl_{CIPW}$ ), such as the secondary-type pyroxenite GV10, have subsolidus phase relations similar to fertile lherzolite. Plagioclase-out boundary is within the pressure range of lherzolites ( $P < 1$  GPa) and spinel is the unique aluminum phase stable at intermediate pressure (1-1.4 GPa). However, in pyroxenites garnet appears at significantly lower pressure than in lherzolite.

**Acknowledgments:** Andrea Risplendente is thanked for technical assistance during the work by electron microprobe. This work was financially supported by the Italian Ministry of Education, University and Research (MIUR) [PRIN-2015C5LN35] "Melt rock reaction and melt migration in the MORB mantle through combined natural and experimental studies".

## References

Adam, J., Green, T. H. & Day, R.A. (1992): An experimental study of two garnet pyroxenite xenoliths from the Bullenmerri and Gnotuk Maars of western Victoria, Australia. *Contrib. Mineral. Petrol.*, **111**, 505–514.

- Aulbach, S. & Jacob, D.E. (2016): Major- and trace-elements in cratonic mantle eclogites and pyroxenites reveal heterogeneous sources and metamorphic processing of low-pressure protoliths. *Lithos*, **262**, 586–605.
- Bodinier, J.-L., Guiraud, M., Fabries, J., Dostal, J. & Dupuy, C. (1987a): Petrogenesis of layered pyroxenites from the Lherz, Freychinede and Prades ultramafic bodies (Ariege, French Pyrenees). *Geochim. Cosmochim. Acta*, **51**, 279–290.
- Bodinier, J.-L., Fabries, J., Lorand, J.-P., Dostal, J. & Dupuy, C. (1987b) : Geochemistry of amphibole pyroxenite veins from the Lherz and Freychinede ultramafic bodies (Ariege, French Pyrenees). *Bull. Mineral.*, **110**, 345–358.
- Bodinier, J.-L. & Godard, M. (2014): Orogenic, ophiolitic and abyssal peridotites. Treatise on Geochemistry 2<sup>nd</sup> Edition, v. 2, H.D. Holland and K.K. Turkian (eds). Oxford, UK, Elsevier Science.
- Borghini, G., Fumagalli, P. & Rampone, E. (2010): The stability of plagioclase in the upper mantle: subsolidus experiments on fertile and depleted lherzolite. *J Petrol*, **51**, 229–254.
- Borghini, G., Fumagalli, P. & Rampone, E. (2011): The geobarometric significance of plagioclase in mantle peridotites: A link between nature and experiments: *Lithos*, **126**, 42–53.
- Borghini, G., Rampone, E., Zanetti, A., Class, C., Cipriani, A., Hofmann, A.W. & Goldstein, S. (2013): Meter-scale Nd isotopic heterogeneity in pyroxenite-bearing Ligurian peridotites encompasses global-scale upper mantle variability. *Geology*, **41**, 1055–1058.
- Borghini, G., Rampone, E., Zanetti, A., Class, C., Cipriani, A., Hofmann, A.W. & Goldstein, S. (2016): Pyroxenite layers in the Northern Apennines upper mantle (Italy) – Generation by pyroxenite melting and melt infiltration. *J. Petrol.*, **57**, 625–653.
- Borghini, G., Fumagalli, P. & Rampone, E. (2017): Partial melting experiments on a natural pyroxenite at 1 and 1.5 GPa: insights on the role of secondary pyroxenites in basalts generation. *Contrib. Mineral. Petrol.*, **172**, 70.
- Brey, G.P., Doroshev, A.M., Gurnis, A.V. & Turkin, A.I. (1999): Garnet–spinel–olivine–orthopyroxene equilibria in the FeO–MgO–Al<sub>2</sub>O<sub>3</sub>–SiO<sub>2</sub>–Cr<sub>2</sub>O<sub>3</sub> system: I. Composition and molar volumes of minerals. *Eur. J. Mineral*, **11**, 599–617.
- Connolly, J.A.D. (1990): Calculation of multivariable phase diagrams: an algorithm based on generalized thermodynamics. *American Journal of Science*, **290**, 666–718.
- Connolly, J.A.D. & Petrini, K. (2002): An automated strategy for calculation of phase diagram sections and retrieval of rock properties as a function of physical conditions. *Journal of Metamorphic Geology*, **20**, 697–708.

517 Fumagalli, P. & Poli, S. (2005): Experimentally determined phase relations in hydrous  
518 peridotites to 6.5 GPa and their consequences on the dynamics of subduction zones. *J.*  
519 *Petrol.*, **45**, 1–24.

520 Fumagalli, P. & Klemme, S. (2015): Mineralogy of the earth: phase transi- tions and  
521 mineralogy of the upper mantle. In: Gerald Schubert (editor-in-chief) Treatise on  
522 Geophysics, vol 2. 2nd edn, Elsevier, Oxford, 7–31.

523 Fumagalli, P., Borghini, G., Rampone, E., Poli, S. (2017): Experimental calibration of  
524 Fosterite-Anorthite-CaTschermak-Enstatite (FACE) geobarometer for mantle peridotites.  
525 *Contrib. Mineral. Petrol.*, **172**, 38.

526 Garrido, C.J. & Bodinier, J-L. (1999): Diversity of mafic rocks in the Ronda peridotite:  
527 evidence for pervasive melt–rock reaction during heating of subcontinental lithosphere by  
528 upwelling asthenosphere. *J. Petrol.*, **40**, 729–754.

529 Gasparik, T. (1984): Two-pyroxene thermobarometry with new experimental data in the  
530 system CaO-MgO-Al<sub>2</sub>O<sub>3</sub>-SiO<sub>2</sub>. *Contrib. Mineral. Petrol.*, **87**, 87–97.

531 Girnis, A.V., Brey, G.P., Doroshev, A.M., Turkin, A.I. & Simon, N. (2003): The system  
532 MgO–Al<sub>2</sub>O<sub>3</sub>–SiO<sub>2</sub>–Cr<sub>2</sub>O<sub>3</sub> revisited: Reanalysis of Doroshev et al. (1997) experiments  
533 and new experiments. *Eur. J. Mineral.*, **15**, 953–964.

534 Gonzaga, R.G., Lowry, D., Jacob, D.E., LeRoex, A., Schulze, D. & Menzies, M.A. (2010):  
535 Eclogites and garnet pyroxenites: similarities and differences. *J. Vol. Geotherm Res.*, **190**,  
536 235–247.

537 Green, D.H. & Ringwood, A.E. (1970): Mineralogy of peridotitic compositions under upper  
538 mantle conditions. *Physics of the Earth and Planetary Interiors*, **3**, 359–371.

539 Green, D.H. & Hibberson, W. (1970): The instability of plagioclase in peridotite at high  
540 pressure. *Lithos*, **3**, 209–221.

541 Green, D.H. & Falloon, T.J. (1998): Pyrolite: A Ringwood concept and its current expression.  
542 In: The Earth's Mantle, eds I. Jackson, 311–378, Cambridge University Press, Cambridge.

543 Gonzaga, R.G., Lowry, D., Jacob, D.E., LeRoex, A., Schulze, D. & Menzies, M.A. (2009):  
544 Eclogites and garnet pyroxenites: similarities and differences. *J. Volcanol. Geotherm. Res.*  
545 **190**, 235–247.

546 Gysi, A.P., Jagoutz, O., Schmidt, M.W. & Targuisti, K. (2011): Petrogenesis of pyroxenites  
547 and melt infiltrations in the ultramafic complex of Beni Boussera, Northern Morocco. *J.*  
548 *Petrol.*, **52**, 1676–1735.

549 Henry, H., Tilhac, R., Griffin, W.L., O'Reilly, S.Y., Satsukawa, T., Kaczmarek, M-A.,  
550 Gregoire, M. & Ceuleneer, G. (2017): Deformation of mantle pyroxenites provides clues

551 to geodynamic processes in subduction zones: case study of the Cabo Ortegal Complex,  
552 Spain. *Earth Planet. Sci. Lett.*, **472**, 174–185.

553 Herzberg, C.T. (1976): The lowest pressure pyrospite garnet-forming reaction in CaO-MgO-  
554 Al<sub>2</sub>O<sub>3</sub>-SiO<sub>2</sub>; the Seiland/Ariegite subfacies boundary in simple spinel-lherzolites. In  
555 Progress in Experimental Petrology, D.3, 235-237. Natural Environment Research  
556 Council Publications, London.

557 Herzberg, C.T. (1978): Pyroxene geothermometry and geobarometry: experimental and  
558 thermodynamic evaluation of some subsolidus phase relations involving pyroxenes in the  
559 system CaO-MgO-Al<sub>2</sub>O<sub>3</sub>-SiO<sub>2</sub>. *Geochim. Cosmochim. Acta*, **42**, 945–957.

560 Hidas, K., Garrido, C., Tommasi, A., Padron-Navarta, J.A., Thielmann, M., Konc, Z., Frets, E.  
561 & Marchesi, C. (2013): Strain localization in pyroxenite by reaction-enhanced softening  
562 in the shallow subcontinental lithospheric mantle. *J. Petrol.*, **54**, 1997–2031.

563 Hirschmann, M.M. & Stolper E.M. (1996): A possible role for garnet pyroxenite in the origin  
564 of the ‘garnet signature’ in MORB. *Contrib. Mineral. Petrol.*, **124**, 185–208.

565 Holland, T.J.B. & Powell, R. (1998): An internally consistent thermo- dynamic data set for  
566 phases of petrological interest. *Journal of Metamorphic Geology*, **16**, 309–343.

567 Irifune, T., Ohtani, E. & Kumazawa, M. (1982): Stability field of khorringite Mg<sub>3</sub>Cr<sub>2</sub>Si<sub>3</sub>O<sub>12</sub> at  
568 high-pressure and its implication to the occurrence of Cr-rich pyrope in the upper mantle.  
569 *Physics of the Earth and Planetary Interiors*, **27**, 263–272.

570 Irving, A.J. (1974): Geochemical and high pressure experimental studies on garnet pyroxenite  
571 and pyroxene granulite xenoliths from the Delegate basaltic pipes. Australia. *J. Petrol.*,  
572 **15**, 1–40.

573 Klemme, S. & O’Neill, H.St.C. (2000): The effect of Cr on the solubility of Al in  
574 orthopyroxene: experiments and thermodynamic modelling. *Contrib. Mineral. Petrol.*,  
575 **140**, 84–98.

576 Klemme, S. (2004): The influence of Cr on the garnet-spinel transition in the Earth’s mantle:  
577 experiments in the system MgO-Cr<sub>2</sub>O<sub>3</sub>-SiO<sub>2</sub> and thermodynamic modelling. *Lithos*, **77**,  
578 639–646.

579 Kinzler, R.J. (1997): Melting of mantle peridotite at pressures approaching the spinel to  
580 garnet transition: Application to mid-ocean ridge basalt petrogenesis. *J. Geophys. Res.*,  
581 **102**, 853–874.

582 Kogiso, T., Hirschmann, M.M., Pertermann, M. (2004): High-pressure partial melting of  
583 mafic lithologies in the mantle. *J. Petrol.*, **45**, 2407–2422.

584 Kushiro, I. & Yoder, H.S. (1966): Anorthite-forsterite and anorthite-enstatite reactions and

585 their bearing on the basalt-eclogite transformation. *J. Petrol.*, **7**, 337–362.  
 586 Lambart, S., Laporte, D., Provost, A., Schiano, P. (2012): Fate of pyroxenite-derived melts in  
 587 the peridotitic mantle: thermodynamic and experimental constraints. *J. Petrol.*, **53**, 451–  
 588 476.  
 589 Lambart, S., Laporte, D. & Schiano, P. (2013): Markers of the pyroxenite contribution in the  
 590 major-element compositions of oceanic basalts: Review of the experimental constraints.  
 591 *Lithos*, **160-161**, 14–36.  
 592 Lambart, S., Baker, M.B. & Stolper, E.M. (2016): The role of pyroxenite in basalt genesis:  
 593 Melt-PX, a melting parameterization for mantle pyroxenites between 0.9 and 5 GPa. *J.*  
 594 *Geophys. Res.*, **121**, 5708–5735.  
 595 Mallik, A. & Dasgupta, R. (2012): Reaction between MORB-eclogite derived melts and  
 596 fertile peridotite and generation of ocean island basalts. *Earth Planet. Sci. Lett.*, **329-330**,  
 597 97–108.  
 598 Milholland, C.S. & Presnall, D.C. (1998): Liquidus phase relations in the CaO–MgO–Al<sub>2</sub>O<sub>3</sub>–  
 599 SiO<sub>2</sub> system at 3.0 GPa: The aluminous pyroxene thermal divide and high-pressure  
 600 fractionation of picritic and komatiitic magmas. *J. Petrol.*, **39**, 3–27.  
 601 Montanini, A., Tribuzio, R. & Anczkiewicz, R. (2006): Exhumation history of a garnet  
 602 pyroxenite-bearing mantle section from a continent-ocean transition (Northern Apennine  
 603 ophiolites, Italy). *J. Petrol.*, **47**, 1943–1971.  
 604 Montanini, A., Tribuzio, R. & Thirlwall, M. (2012): Garnet clinopyroxenite layers from the  
 605 mantle sequences of the Northern Apennine ophiolites (Italy): Evidence for recycling of  
 606 crustal material. *Earth Planet. Sci. Lett.*, **351-352**, 171–181.  
 607 Montanini, A. & Tribuzio, R. (2015): Evolution of recycled crust within the mantle:  
 608 constraints from the garnet pyroxenites of the External Ligurian ophiolites (northern  
 609 Apennines, Italy). *Geology*, **43**, 911–914.  
 610 Morishita, T. & Arai, S. (2001): Petrogenesis of corundum-bearing mafic rock in the  
 611 Horoman Peridotite Complex, Japan. *J. Petrol.*, **42**, 1279–1299.  
 612 Nickel, K.G. (1986) Phase equilibria in the system SiO<sub>2</sub>–MgO–Al<sub>2</sub>O<sub>3</sub>–CaO–Cr<sub>2</sub>O<sub>3</sub>  
 613 (SMACCr) and their bearing on spinel garnet lherzolite relationships. *Neues Jahrbuch*  
 614 *fu r Mineralogie Abhandlungen*, **155**, 259–287.  
 615 Niida, K. & Green, D. H. (1999): Stability and chemical composition of pargasitic amphibole  
 616 in MORB pyrolite under upper mantle conditions. *Contrib. Mineral. Petrol.*, **135**, 18–40.  
 617 Obata, M. (1976): The solubility of Al<sub>2</sub>O<sub>3</sub> in orthopyroxenes in spinel and plagioclase  
 618 peridotites and spinel pyroxenite. *Am. Mineral.*, **61**, 804–816.

- O'Hara, M.J., Richardson, S.W. & Wilson, G. (1971): Garnet-peridotite stability and occurrence in crust and mantle. *Contrib. Mineral. Petrol.*, **32**, 48–68.
- O'Neill, H.St.C. (1981): The transition between spinel lherzolite and garnet lherzolite, and its use as a geobarometer. *Contrib. Mineral. Petrol.*, **77**, 185–194.
- Phipps Morgan, J. (2001): Thermodynamics of pressure release melting of a veined plum pudding mantle. *Geochem. Geophys. Geosyst.*, **2**, 2000GC000049.
- Rampone, E., Hofmann, A.W., Piccardo, G.B., Vannucci, R., Bottazzi, P. & Ottolini, L. (1995): Petrology, mineral and isotope geochemistry of the External Liguride peridotites (Northern Apennines, Italy). *J. Petrol.*, **123**, 61–76.
- Robinson, J.A.C., Wood, B.J. & Blundy, J.D. (1998): The beginning of melting of fertile and depleted peridotite at 1.5 GPa. *Earth Planet. Sci. Lett.*, **155**, 97–111.
- Schmadicke, E. (2000): Phase relations in peridotitic and pyroxenitic rocks in the model system CMASH and NCMASH. *J. Petrol.*, **41**, 69–86.
- Shorttle, O. & MacLennan, J. (2011): Compositional trends of Icelandic basalts: implications for short-length scale lithological heterogeneity in mantle plumes. *Geochem. Geophys. Geosyst.*, **12**, Q11008.
- Sobolev, A.V., Hofmann, A.W., Sobolev, S.V., Nikogosian, I.K. (2005): An olivine-free mantle source of Hawaiian shield basalts. *Nature*, **434**, 590–597.
- Sobolev, A.V., Hofmann, A.W., Kuzmin, D.V., Yaxley, G.M., Arndt, N.T., Chung, S-L., Danyushevsky, L.V., Elliott, T., Frey, F.A., Garcia, M.O., Gurenko, A.A., Kamenetsky, V.S., Kerr, A.C., Krivolutsкая, N.A., Matvienkov, V.V., Nikogosian, I.K., Rocholl, A., Sigurdsson, I.A., Sushchevskaya, N.M. & Teklay, M. (2007): The amount of recycled crust in sources of mantle-derived melts. *Science*, **316**, 412–417.
- Takazawa, E., Frey, F.A., Shimizu, N., Saal, N. & Obata, M. (1999): Polybaric petrogenesis of mafic layers in the Horoman peridotite complex, Japan. *J. Petrol.* **40**, 1827–1831.
- Ulmer, P. & Luth, R.W. (1991): The graphite fluid equilibrium in P, T, fO<sub>2</sub> space: an experimental determination to 30 kbar and 1600°C. *Contrib. Mineral. Petrol.*, **106**, 265–272.
- Van Acken, D., Becker, H., Walker, R.J., McDonough, W.F., Wombacher, F., Ash, R.D. & Piccoli, P.M. (2010): Formation of pyroxenite layers in the Totalp ultramafic massif (Swiss Alps) – Insights from highly siderophile elements and Os isotopes. *Geochim. Cosmochim. Acta*, **74**, 661–683.
- Walter, M.J. & Presnall, D.C. (1994): Melting behaviour of simplified lherzolite in the system CaO-MgO-Al<sub>2</sub>O<sub>3</sub>-SiO<sub>2</sub>-Na<sub>2</sub>O from 7 to 35 kbar. *J. Petrol.*, **35**, 329–359.

Walter, M.J. (1998): Melting of garnet peridotite and the origin of komatiite and depleted lithosphere. *J. Petrol.*, **39**, 29–60.

Walter, M., Katsura, T., Kubo, A., Shinmei, T., Nishikawa, O., Ito, E., Leshner, C. & Funakoshi, K. (2002): Spinel-garnet lherzolite transition in the system CaO-MgO-Al<sub>2</sub>O<sub>3</sub>-SiO<sub>2</sub> revisited: an in situ X-ray study. *Geochim. Cosmochim. Acta*, **66**, 2109–2121.

Webb, S.A.C. & Wood, B.J. (1986): Spinel-pyroxene-garnet relationships and their dependence on Cr/Al ratio. *Contrib. Mineral. Petrol.*, **92**, 471–480.

Yaxley, G.M. & Green, D.H. (1998): Reactions between eclogite and peridotite: mantle refertilisation by subduction of oceanic crust. *Schweiz. Mineral. Petrogr. Mitt.*, **78**, 243–255.

Zibera, L., Klemme, S. & Nimis, P. (2013): Garnet and spinel in fertile and depleted mantle: insights from thermodynamic modelling. *Contrib. Mineral. Petrol.*, **166**, 411–421.

## FIGURE CAPTIONS

**Figure 1.** Phase assemblages in pyroxenite GV10 as a function of pressure and temperature. Also reported is the solidus curve, the plagioclase-out and garnet-in boundaries.

**Figure 2.** Representative textures in subsolidus experiments on pyroxenite GV10. (a) Back-scattered electron (BSE) image of experiments GV10-83-23 (0.8 GPa; 1100°C): plagioclase-bearing assemblage is composed of clinopyroxene, orthopyroxene, olivine, plagioclase and Cr-spinel. (b) BSE image of run GV10-83-12 (1.3 GPa; 1150°C), showing the spinel-facies assemblage. (c) BSE image of run GV10-83-7 (1.5 GPa; 1200°C), in which a coarse seed of spinel is partially substituted by fine-grained garnet-bearing mineral assemblage.

**Figure 3.** BSE image and X-ray maps for Si, Al and Ca of a representative texture in run GV10-83-7 (1.5 GPa; 1200°C), showing a large garnet seed partially replaced by a newly formed mineral assemblage in which are evidenced new small spinel and garnet grains.

**Figure 4.** Al content (a.p.f.u.) variations in clinopyroxenes (a) and orthopyroxene (b) as a function of pressure. Numbers close to symbols refer to run temperature. The blue and green curves correspond to the Al variation trend in pyroxenes, calculated for the pyroxenite GV10 composition using Perple\_X software (Connolly, 1990; Connolly & Petrini, 2002), at 1100 and 1200°C, respectively.

**Figure 5.**  $X_{An}$  (Ca/(Ca+Na)) in plagioclase vs.  $X_{Al}^{M1}$  in clinopyroxene in experiments on pyroxenite GV10 (blue circles) compared to experimental data from previous studies on lherzolites (Fumagalli et al., 2017, and references therein).

**Figure 6.** Modal abundances as a function of pressure in experiments on GV10 at 1100°C (0.7-1.0 GPa), and 1150°C (1.3-1.5 GPa). Modal amounts of experiments at 0.7 GPa, 1100°C, have been computed by using olivine and spinel compositions from experiments at 0.8 GPa, 1100°C. The grey bands represent the pressure of plagioclase-out and garnet-in boundaries for pyroxenite GV10.

**Figure 7.** Schematic chemography for the system Cr-FNCMAS, constructed projecting from exchange vectors CaAlNa-1Si-1, MgFe-1 and AlCr-1 into the compositional space (Mg,Fe)O-CaO\*-SiO<sub>2</sub>-(Al,Cr)<sub>2</sub>O<sub>3</sub>. Stars represent the bulk compositions of websterite GV10 (this study), clinopyroxenite DR9734 (Adam et al., 1992) and fertile lherzolite FLZ (Borghini et al., 2010). CIPW normative plagioclase (Pl<sub>CIPW</sub>) for each bulk composition is reported in empty circles. Compositions of mineral phases are from experiments on websterite GV10 (green circles, this study) and on clinopyroxenite DR9734 (orange circles, Adam et al. 1992).

**Figure 8.** The plagioclase-out boundary and solidus curves determined by this experimental study on pyroxenite GV10 and previously investigated lherzolite bulks: Hawaiian pyrolite, HPY (Green & Ringwood, 1970); fertile and depleted lherzolites, FLZ and DLZ (Borghini et al., 2010); high-Na fertile lherzolite, HNa-FLZ (Fumagalli et al., 2017). The blue dashed curve represents the plagioclase-out boundary derived by thermodynamic calculations using Perple\_X package (Connolly, 1990; Connolly & Petrini, 2002), in the model chemical system Cr-NCFMAS. In empty circles the values of normative Ab/Di and X<sub>Cr</sub> for each bulk composition are indicated.

**Figure 9.** The garnet-in curves experimentally determined for: pyroxenite GV10 (this study); MORB pyrolite (hMPY) modeled in the hydrous Cr-Ti-bearing system from Green and Ringwood (1970); model hawaiian peridotite nodule (PX) studied by Fumagalli & Poli (2005); lherzolite in CMAS system by Klemme & O'Neill (2000) and Walter et al. (2002). The blue dashed curve represents the garnet-in curve derived by thermodynamic calculations using Perple\_X package (Connolly, 1990; Connolly & Petrini, 2002), in the model chemical system Cr-NCFMAS.

Figure 1

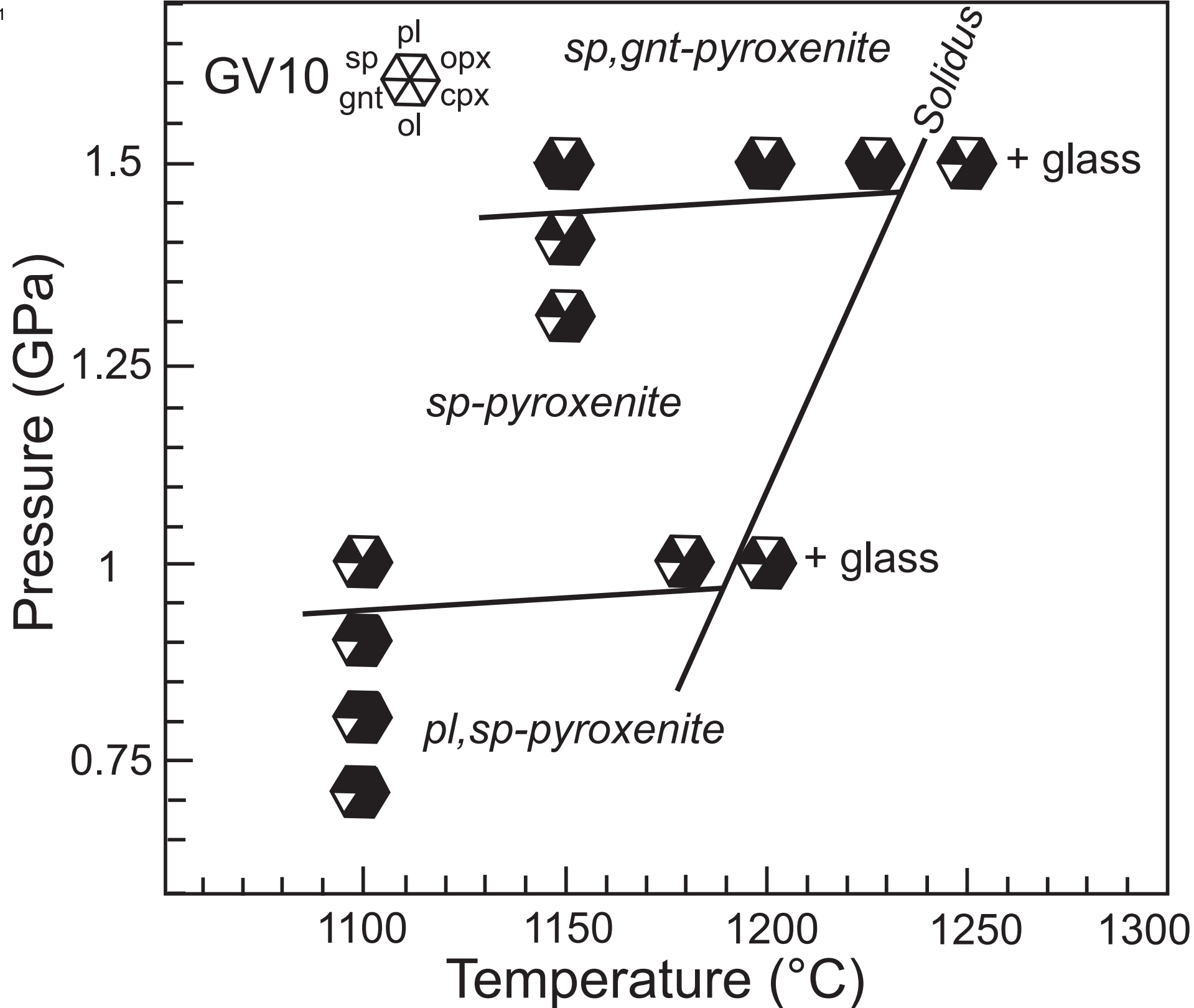


Figure2

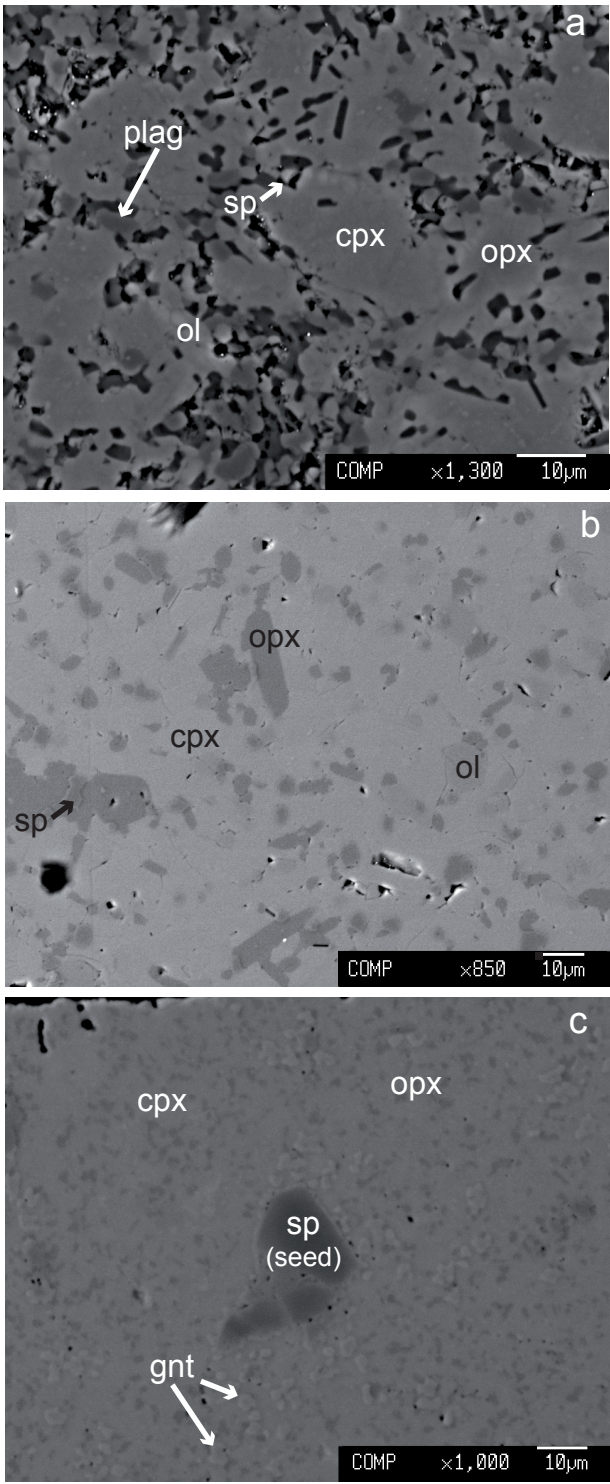


Figure3

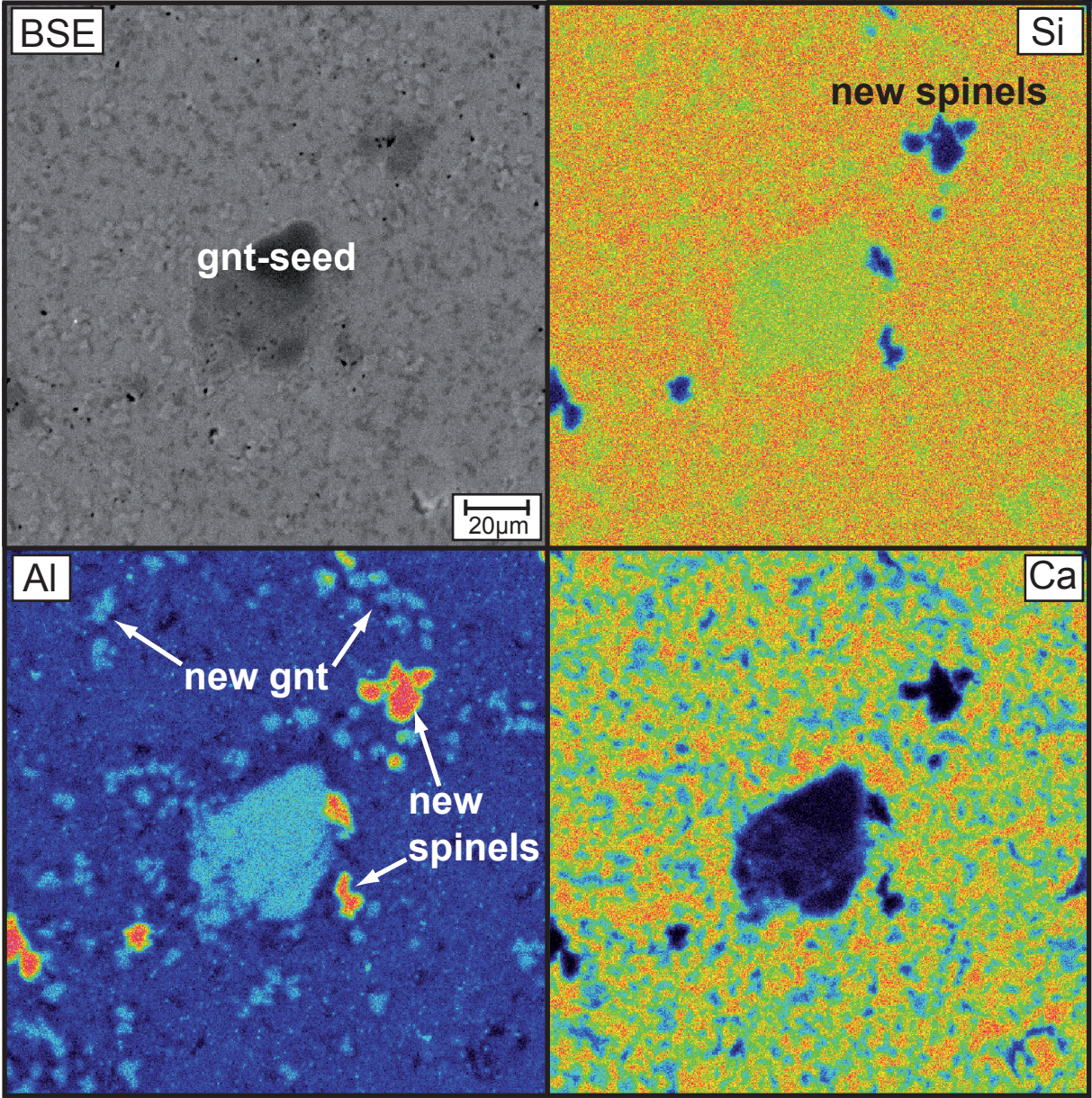


Figure 4

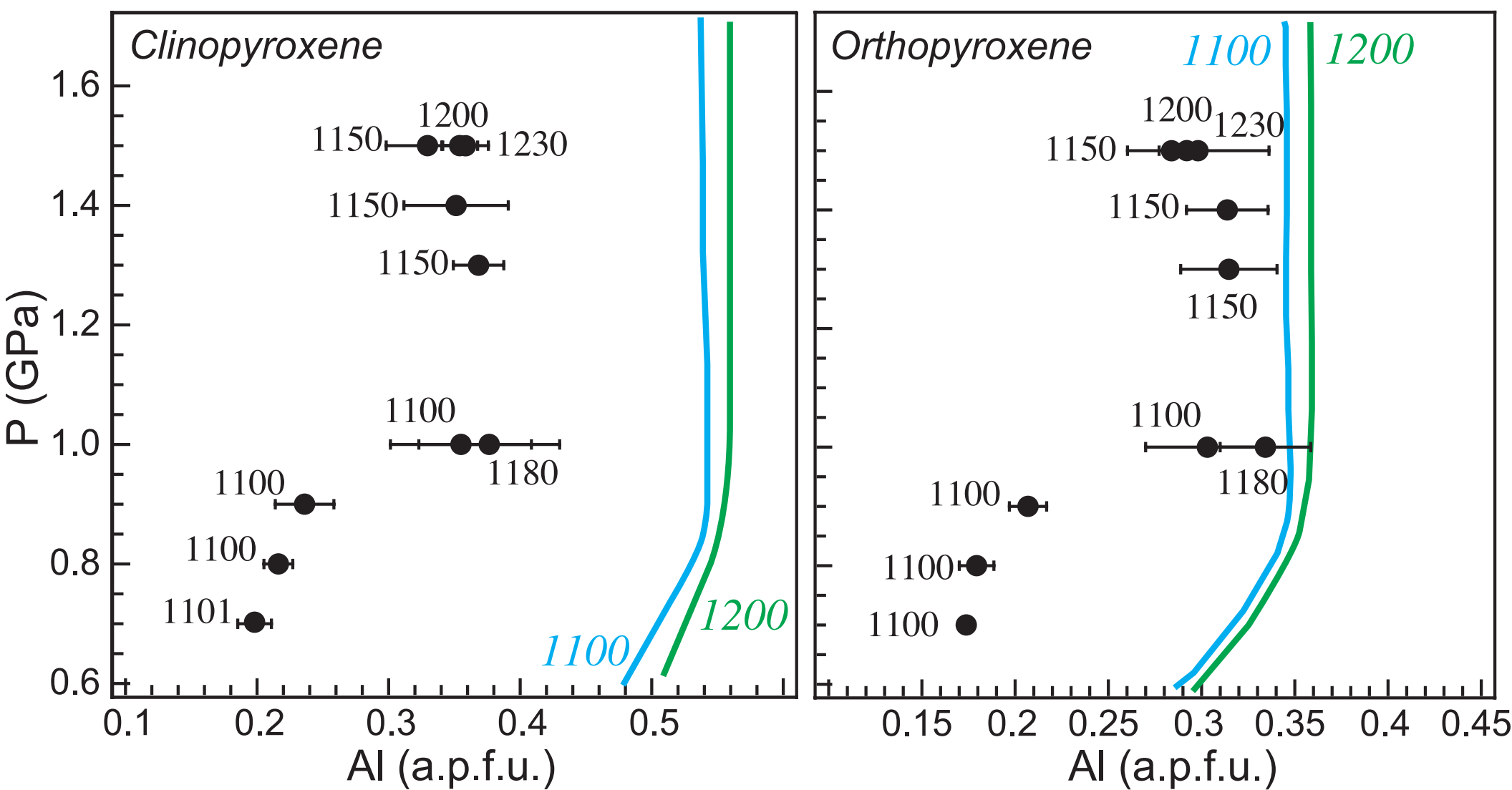


Figure5

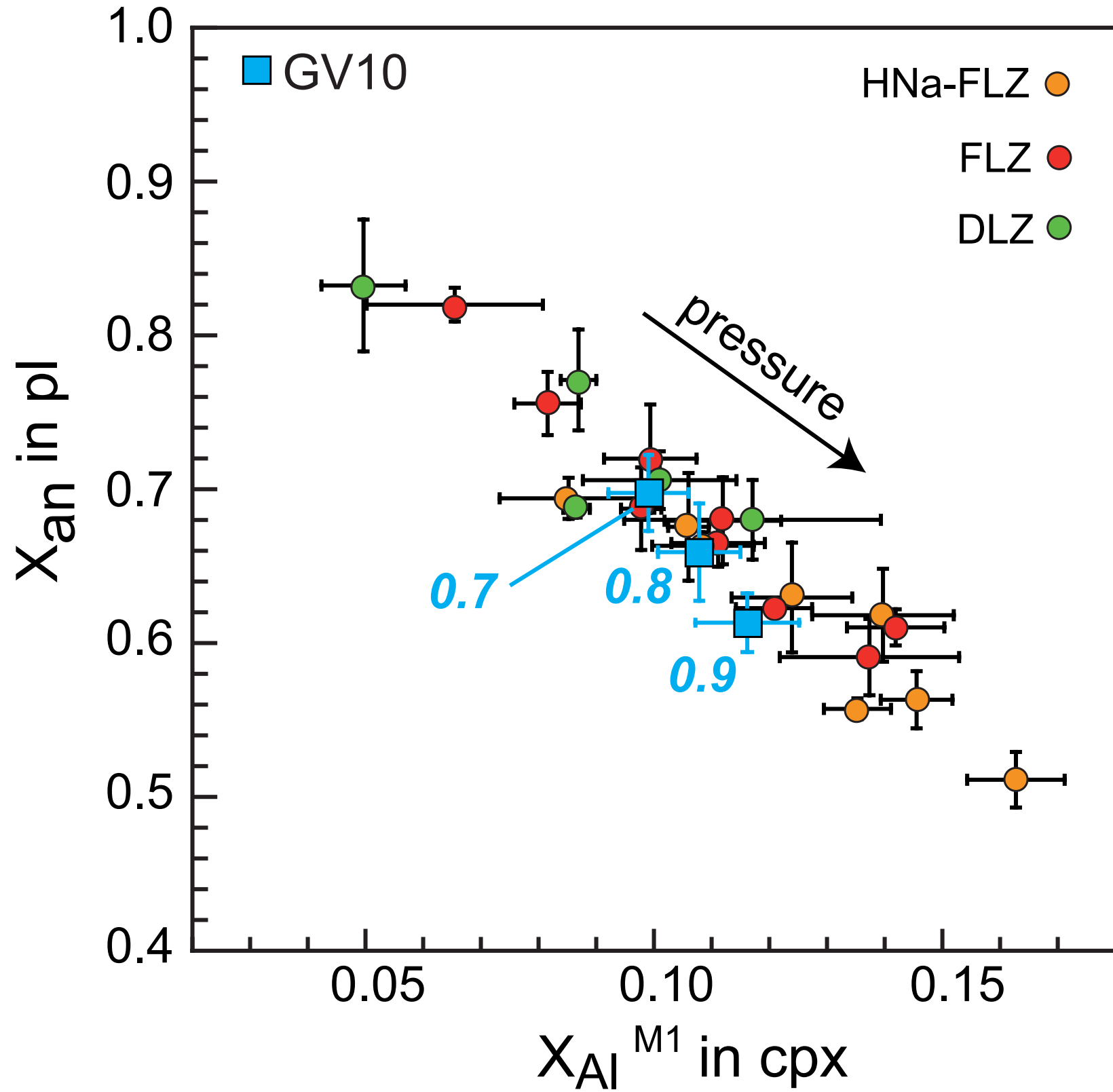


Figure6

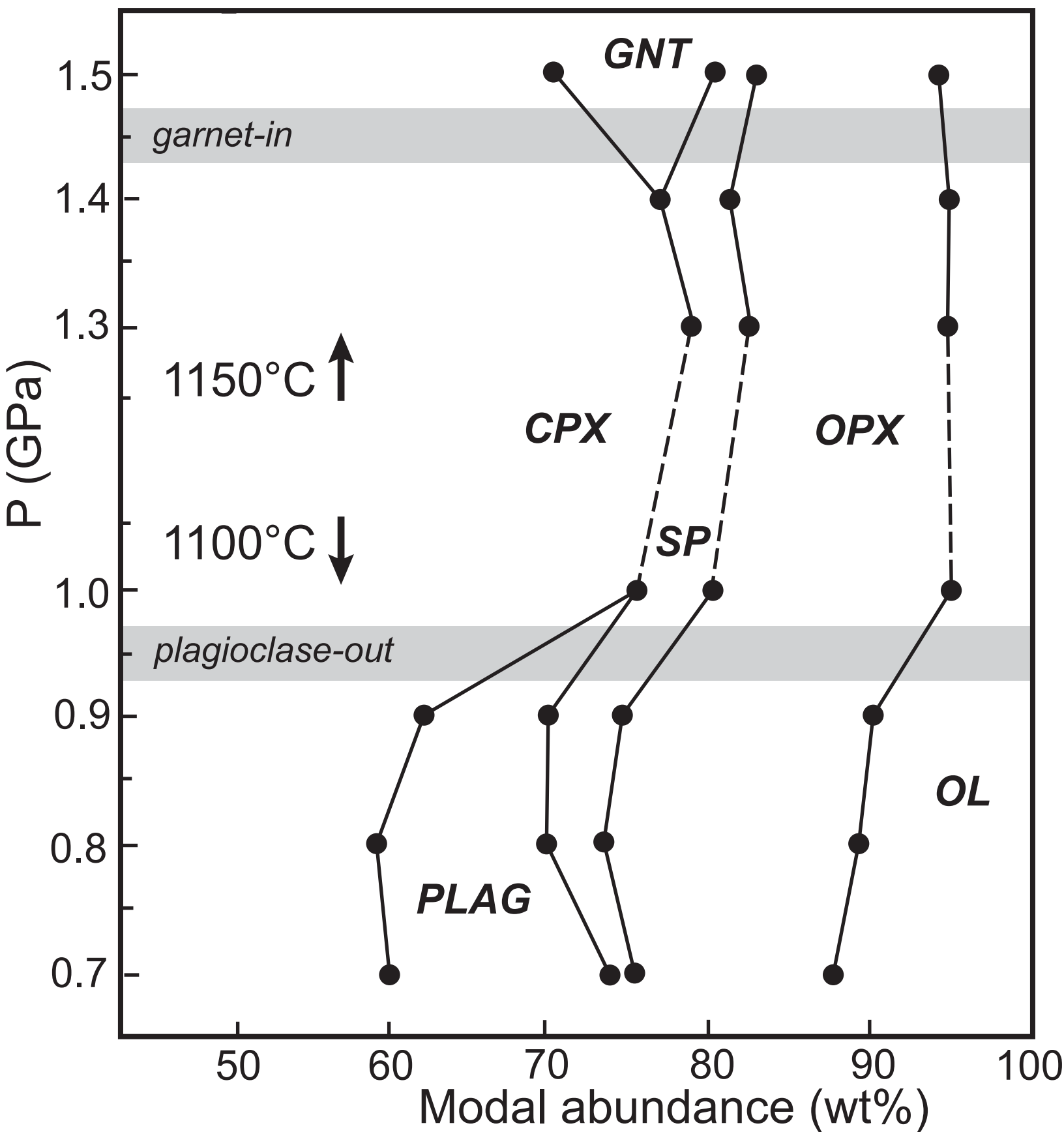


Figure 7

1 GPa, 1000 - 1100°C

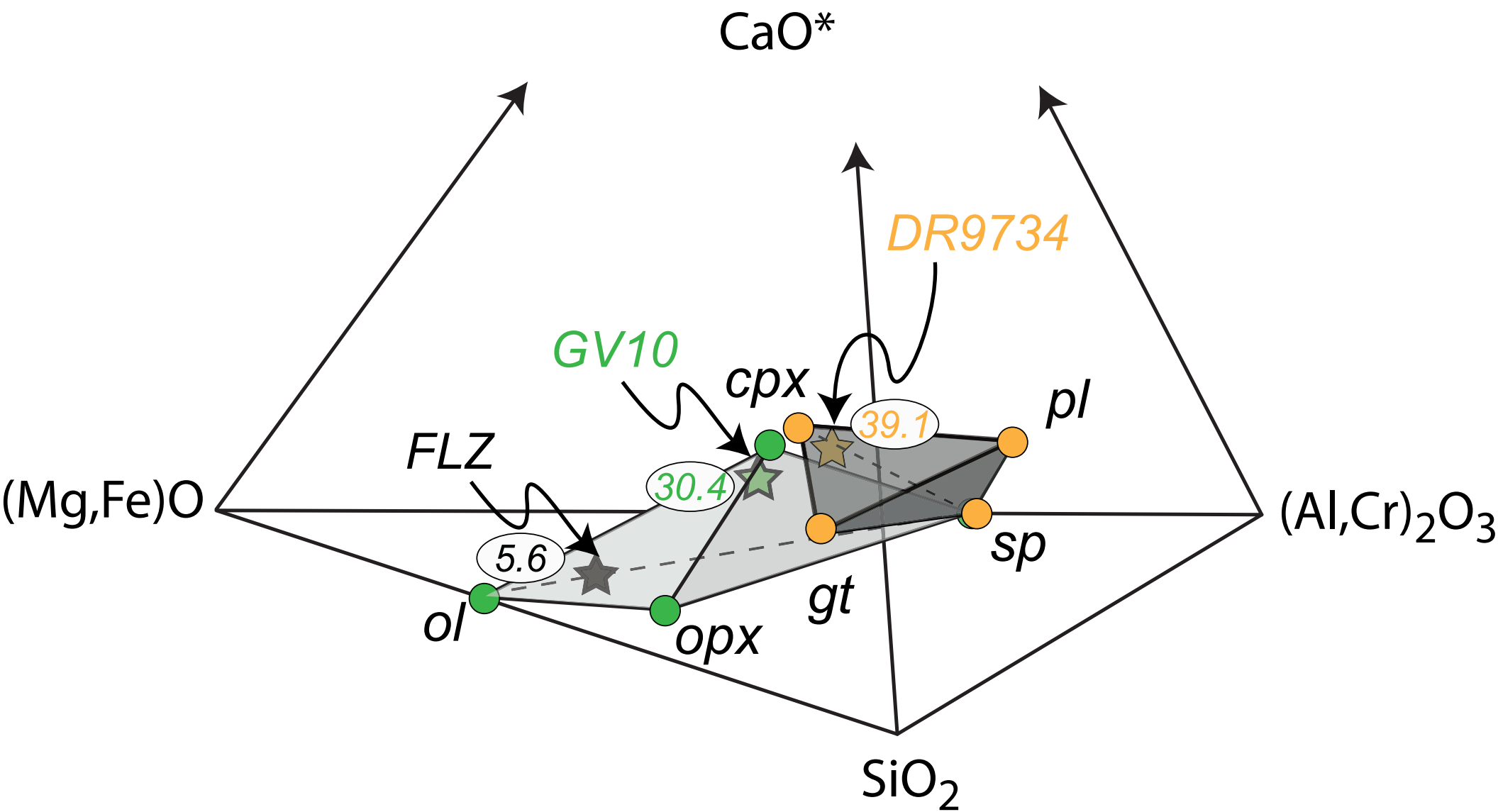


Figure8

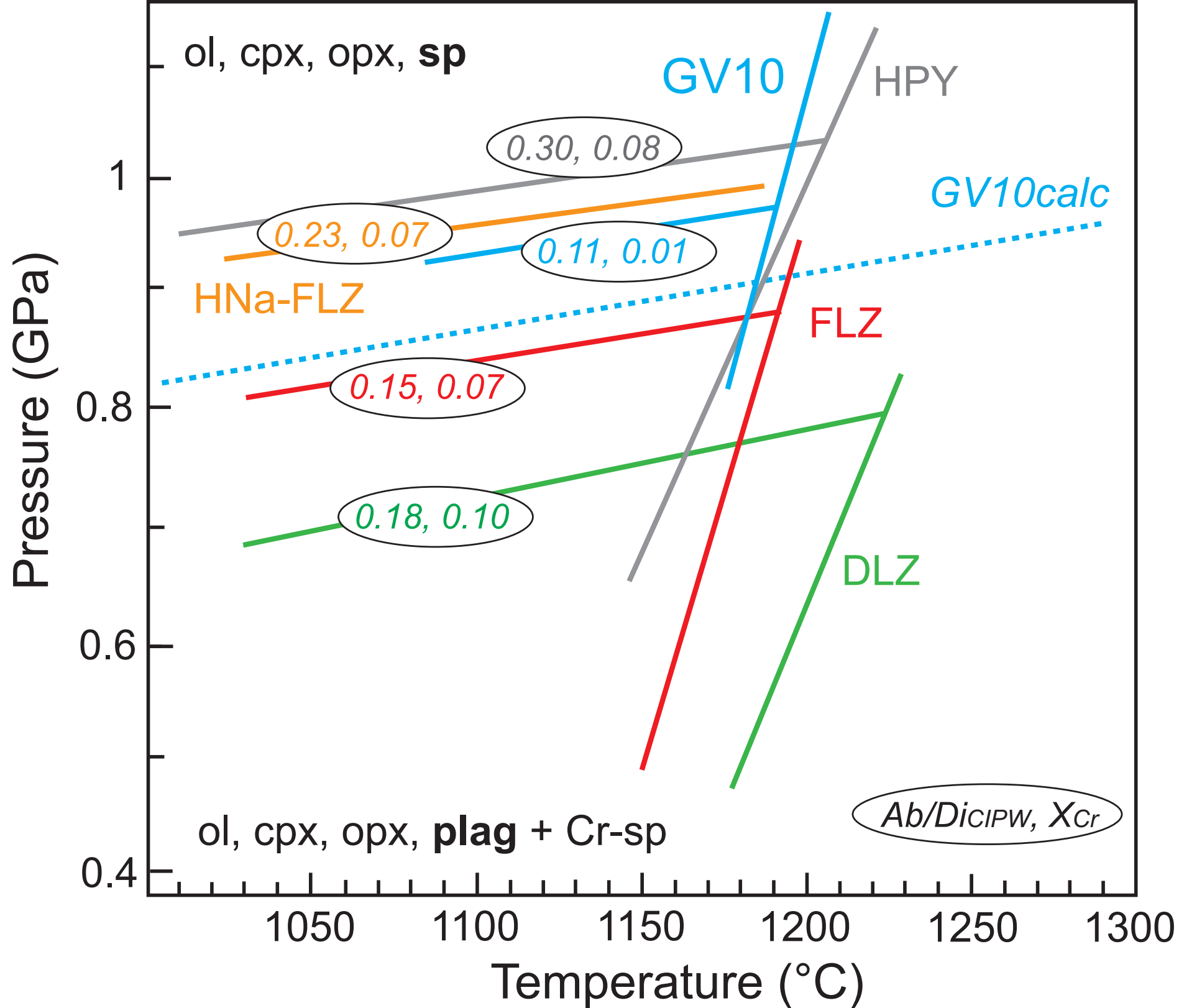


Figure9

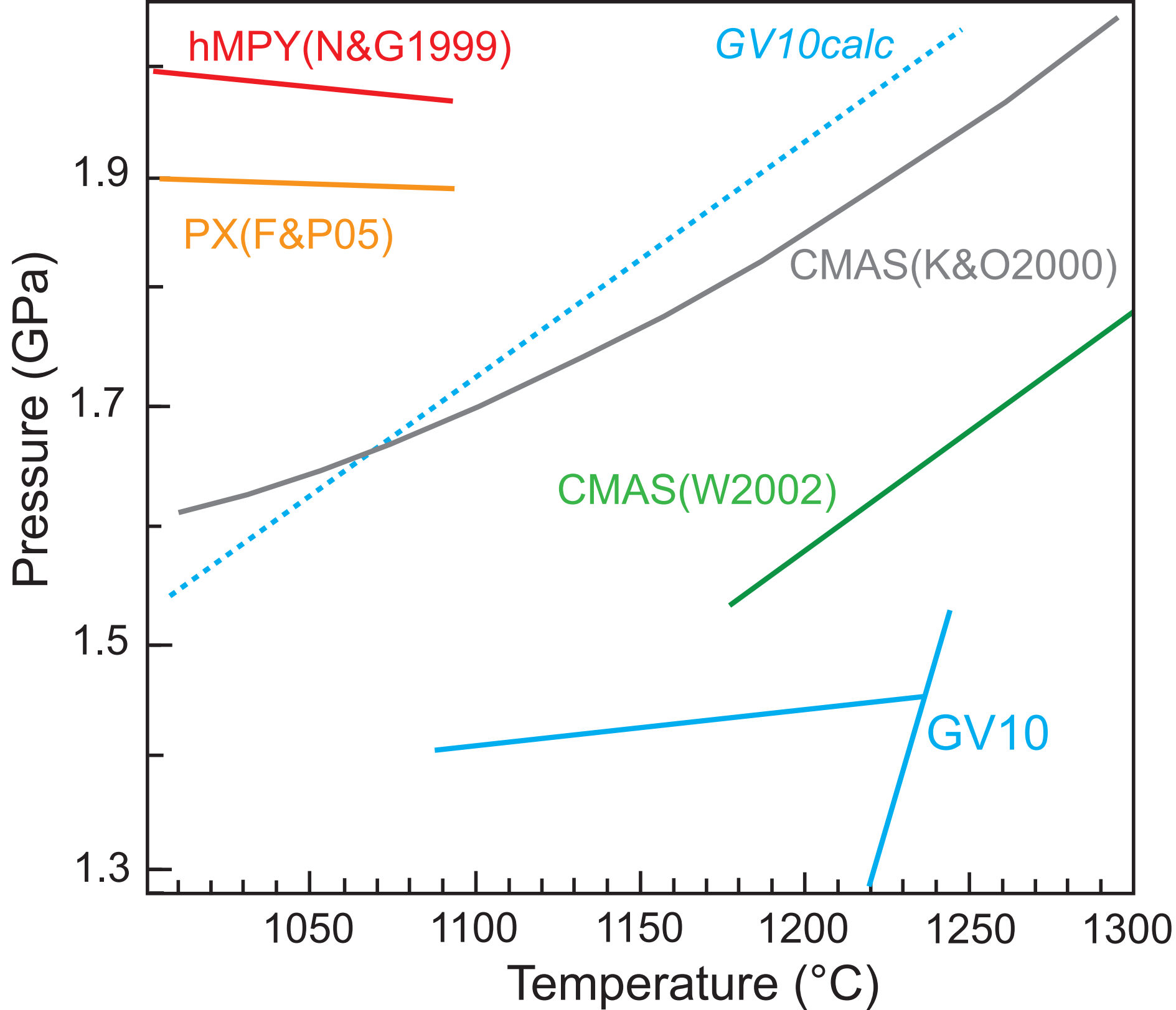


Table1

Table 1. Compositions of starting material of this work and previous studies

	GV10*	GV10	DR9734	DR10165	R392	R394	R130	R698
	rock an.	glass	1 sigma	Adam et al. (1992)		Irving (1974)		
SiO <sub>2</sub>	47.54	47.57 (12)		47.31	46.02	46.54	45.73	47.24
TiO <sub>2</sub>	0.45	0.45 (6)		0.23	0.39	0.45	0.69	2.10
Al <sub>2</sub> O <sub>3</sub>	10.27	10.39 (6)		14.95	13.57	15.48	14.29	15.71
Cr <sub>2</sub> O <sub>3</sub>	0.16	0.15 (4)		0.09	0.41	0.16	0.05	0.00
FeO	7.23	6.99 (11)		6.52	7.61	6.29	5.26	11.49
MnO	0.17	0.18 (6)		0.14	0.12	0.15	0.16	0.19
MgO	19.15	19.23 (14)		12.83	19.58	15.38	18.25	8.21
CaO	14.43	14.49 (9)		16.44	11.67	14.28	14.68	11.61
Na <sub>2</sub> O	0.50	0.48 (2)		1.44	0.63	0.96	0.81	3.20
K <sub>2</sub> O	0.10	0.08 (2)		0.03	0.00	0.26	0.04	0.24
Tot.	100.00	100.00		100.00	100.00	100.00	100.00	100.00
X <sub>Mg</sub>	0.83	0.83 (25)		0.78	0.82	0.81	0.86	0.56
X <sub>Cr</sub>	0.01	0.01 (1)		0.00	0.02	0.01	0.00	0.00
(mol%)								
Ab	4.23	4.06		4.61	5.73	6.21	2.36	18.19
An	25.56	26.04		34.35	37.00	37.32	35.37	27.83
Di	36.88	36.71		38.06	20.00	27.00	29.90	24.59
Hy	4.32	4.68			19.05			
Ol	27.48	27.09		18.22	17.33	26.00	28.40	19.11
Il	0.85	0.85		0.44	0.80	0.85	1.31	3.99
Cm	0.24	0.24		0.15	0.40	0.24	0.16	
Or	0.59	0.47		0.18		1.54	0.24	1.41
Nf				4.10		1.04	2.44	4.86
Ab/Di	0.11	0.11		0.12	0.29	0.23	0.08	0.74

All compositions are normalized to a sum of 100%. In the third column, in parentheses we report the errors (1σ) given in terms of least unit cited; e.g. 47.57 (12) and 0.45 (6) represent 47.57 + 0.12 and 0.45 + 0.06, respectively.  
(\*) Major element analysis by lithium metaborate/tetraborate fusion ICP on powder samples GV10 (Borghini et al., 2016).  
CIPW norms (%mol proportions) are also reported. Ab, albite; An, anorthite; Di, diopside; Hy, hypersthene; Ol, olivine; Il, ilmenite; Cm, chromite; Or, orthoclase; Nf, nepheline.

Table 2. Experimental run conditions and products

Run	P (GPa)	T (°C)	t (h)	Run products
GV10-83-25	0.7	1100	416	cpx, opx, sp, plag, ol
GV10-83-23	0.8	1100	495	cpx, opx, sp, plag, ol
GV10-83-24	0.9	1100	453	cpx, opx, sp, plag, ol
GV10-83-5	1	1100	408	cpx, opx, sp, ol
GV10-83-4*	1	1180	240	cpx, opx, sp, ol
GV10-83-1*	1	1200	120	glass, cpx, ol, opx, sp
GV10-83-12	1.3	1150	336	cpx, opx, sp, ol
GV10-83-17	1.4	1150	311	cpx, opx, sp, ol
GV10-83-3	1.5	1150	357	cpx, opx, gnt, sp, ol
GV10-83-7	1.5	1200	162	cpx, opx, gnt, sp, ol
GV10-83-16*	1.5	1230	94	cpx, opx, ol, sp, gnt
GV10-83-9*	1.5	1250	155	glass, cpx, ol, opx, sp

(\*) from Borghini et al. (2017)

Table3

Table 3. Representative compositions of clinopyroxenes

Run:	GV10-83-25	GV10-83-23	GV10-83-24	GV10-83-5	GV10-83-4*	GV10-83-12	GV10-83-17	GV10-83-3	GV10-83-7	GV10-83-16*
P(GPa)	0.7	0.8	0.9	1	1	1.3	1.4	1.5	1.5	1.5
T(°C)	1100	1100	1100	1100	1180	1150	1150	1150	1200	1230
No. An	5	6	15	6	15	9	11	5	10	11
SiO <sub>2</sub>	51.43 (0.43)	51.00 (0.32)	50.92 (0.30)	49.78 (1.57)	49.98 (0.89)	50.32 (0.43)	50.35 (0.84)	50.46 (0.63)	50.50 (0.37)	50.48 (0.32)
TiO <sub>2</sub>	0.34 (0.06)	0.36 (0.10)	0.51 (0.06)	0.53 (0.06)	0.34 (0.23)	0.51 (0.04)	0.54 (0.06)	0.51 (0.04)	0.49 (0.06)	0.50 (0.08)
Al <sub>2</sub> O <sub>3</sub>	4.59 (0.29)	4.99 (0.26)	5.47 (0.53)	8.24 (1.17)	8.79 (1.24)	8.65 (0.44)	8.23 (0.92)	7.69 (0.76)	8.32 (0.33)	8.43 (0.42)
Cr <sub>2</sub> O <sub>3</sub>	0.20 (0.06)	0.20 (0.02)	0.20 (0.05)	0.14 (0.05)	0.12 (0.04)	0.13 (0.03)	0.13 (0.04)	0.13 (0.04)	0.13 (0.04)	0.12 (0.04)
FeO	4.84 (0.06)	5.31 (0.33)	5.23 (0.46)	5.56 (0.65)	5.47 (0.28)	5.93 (0.19)	5.68 (0.40)	5.24 (0.13)	5.56 (0.21)	5.65 (0.16)
MgO	16.18 (0.15)	15.80 (0.46)	15.56 (0.36)	15.87 (0.87)	15.91 (0.41)	16.45 (0.27)	16.41 (0.31)	16.03 (0.28)	16.88 (0.44)	17.11 (0.21)
CaO	21.99 (0.12)	21.66 (0.38)	21.78 (0.40)	18.97 (1.56)	19.00 (0.56)	18.05 (0.26)	18.52 (0.83)	19.53 (0.45)	18.10 (0.76)	17.74 (0.32)
Na <sub>2</sub> O	0.29 (0.04)	0.21 (0.06)	0.24 (0.05)	0.42 (0.04)	0.40 (0.06)	0.40 (0.04)	0.38 (0.05)	0.43 (0.06)	0.37 (0.05)	0.36 (0.03)
Total	99.84 (0.37)	99.53 (0.54)	99.92 (0.38)	99.50 (1.14)	100.03 (0.51)	100.45 (0.47)	100.24 (0.45)	100.02 (0.61)	100.35 (0.22)	100.39 (0.22)
Si	1.885 (0.009)	1.876 (0.012)	1.865 (0.012)	1.820 (0.040)	1.815 (0.029)	1.818 (0.009)	1.824 (0.025)	1.834 (0.023)	1.824 (0.011)	1.821 (0.013)
Ti	0.009 (0.002)	0.010 (0.003)	0.014 (0.002)	0.015 (0.002)	0.009 (0.006)	0.014 (0.001)	0.015 (0.002)	0.014 (0.001)	0.013 (0.002)	0.014 (0.002)
Al	0.198 (0.013)	0.216 (0.011)	0.236 (0.022)	0.355 (0.054)	0.376 (0.054)	0.368 (0.019)	0.351 (0.040)	0.330 (0.031)	0.354 (0.014)	0.358 (0.017)
Cr	0.006 (0.002)	0.006 (0.001)	0.006 (0.001)	0.004 (0.002)	0.003 (0.001)	0.004 (0.001)	0.004 (0.001)	0.004 (0.001)	0.004 (0.001)	0.003 (0.001)
Fe	0.148 (0.002)	0.163 (0.010)	0.160 (0.014)	0.171 (0.020)	0.166 (0.008)	0.179 (0.006)	0.172 (0.012)	0.159 (0.003)	0.168 (0.006)	0.171 (0.005)
Mg	0.884 (0.008)	0.866 (0.023)	0.850 (0.018)	0.865 (0.049)	0.861 (0.022)	0.886 (0.014)	0.886 (0.016)	0.869 (0.015)	0.908 (0.022)	0.920 (0.011)
Ca	0.863 (0.006)	0.854 (0.018)	0.855 (0.017)	0.743 (0.057)	0.739 (0.022)	0.699 (0.009)	0.719 (0.033)	0.761 (0.019)	0.700 (0.031)	0.686 (0.013)
Na	0.020 (0.003)	0.016 (0.004)	0.018 (0.004)	0.030 (0.003)	0.028 (0.004)	0.028 (0.003)	0.027 (0.004)	0.030 (0.004)	0.026 (0.004)	0.025 (0.002)
Cat.Sum.	4.014 (0.005)	4.008 (0.010)	4.004 (0.007)	4.002 (0.014)	4.000 (0.007)	3.996 (0.004)	3.997 (0.007)	4.000 (0.007)	3.997 (0.006)	3.997 (0.005)
X <sub>Mg</sub>	0.857 (0.002)	0.841 (0.008)	0.841 (0.014)	0.836 (0.011)	0.838 (0.008)	0.832 (0.005)	0.837 (0.009)	0.845 (0.002)	0.844 (0.003)	0.844 (0.003)

X<sub>Mg</sub> = Mg/(Mg+Fe<sup>tot</sup>). Numbers in parentheses correspond to 1sigma standard deviations. Cations are calculated on the basis of 6 oxygens and all Fe = Fe<sup>2+</sup>.

Table4

Table 4. Representative compositions of orthopyroxenes

Run:	GV10-83-25	GV10-83-23	GV10-83-24	GV10-83-5	GV10-83-4*	GV10-83-12	GV10-83-17	GV10-83-3	GV10-83-7	GV10-83-16*
P(GPa)	0.7	0.8	0.9	1	1	1.3	1.4	1.5	1.5	1.5
T(°C)	1100	1100	1100	1100	1180	1150	1150	1150	1200	1230
No. An	4	6	5	10	9	7	8	9	7	9
SiO <sub>2</sub>	54.62 (0.37)	54.91 (0.34)	54.45 (0.39)	52.26 (0.53)	51.55 (0.77)	52.56 (0.56)	52.49 (0.58)	53.11 (0.19)	53.07 (0.11)	52.33 (0.69)
TiO <sub>2</sub>	0.17 (0.04)	0.13 (0.07)	0.11 (0.06)	0.21 (0.05)	0.21 (0.05)	0.22 (0.03)	0.20 (0.02)	0.17 (0.03)	0.20 (0.02)	0.28 (0.17)
Al <sub>2</sub> O <sub>3</sub>	4.22 (0.09)	4.35 (0.24)	5.03 (0.22)	7.29 (0.79)	8.02 (0.54)	7.67 (0.62)	7.63 (0.52)	6.85 (0.17)	7.08 (0.16)	7.19 (0.91)
Cr <sub>2</sub> O <sub>3</sub>	0.10 (0.02)	0.08 (0.01)	0.15 (0.04)	0.13 (0.04)	0.14 (0.03)	0.10 (0.04)	0.06 (0.04)	0.06 (0.03)	0.06 (0.03)	0.08 (0.06)
FeO	9.49 (0.26)	9.60 (0.34)	9.63 (0.25)	9.61 (0.25)	9.47 (0.32)	9.62 (0.12)	9.54 (0.12)	9.19 (0.23)	9.14 (0.24)	9.23 (0.14)
MgO	30.00 (0.20)	29.61 (0.36)	29.64 (0.44)	28.49 (0.30)	28.16 (0.25)	28.69 (0.14)	28.48 (0.13)	28.74 (0.29)	28.95 (0.30)	28.82 (0.40)
CaO	1.78 (0.18)	1.46 (0.37)	1.32 (0.13)	1.56 (0.13)	1.93 (0.68)	1.92 (0.06)	1.81 (0.09)	1.41 (0.11)	1.51 (0.09)	1.82 (0.09)
Na <sub>2</sub> O	0.05 (0.04)	0.08 (0.02)	0.04 (0.03)	0.05 (0.03)	0.04 (0.03)	0.05 (0.02)	0.05 (0.03)	0.05 (0.03)	0.05 (0.02)	0.05 (0.02)
Total	100.41 (0.27)	100.22 (0.44)	100.38 (0.46)	99.60 (0.66)	99.53 (0.79)	100.84 (0.29)	100.27 (0.30)	99.56 (0.24)	100.05 (0.42)	99.81 (0.57)
Si	1.909 (0.008)	1.920 (0.014)	1.901 (0.011)	1.844 (0.014)	1.822 (0.015)	1.829 (0.018)	1.831 (0.017)	1.866 (0.007)	1.857 (0.006)	1.841 (0.023)
Ti	0.004 (0.001)	0.003 (0.002)	0.003 (0.002)	0.006 (0.001)	0.006 (0.001)	0.006 (0.001)	0.005 (0.001)	0.004 (0.001)	0.005 (0.001)	0.007 (0.004)
Al	0.174 (0.004)	0.179 (0.009)	0.207 (0.010)	0.303 (0.033)	0.334 (0.024)	0.315 (0.026)	0.314 (0.022)	0.284 (0.007)	0.292 (0.006)	0.298 (0.038)
Cr	0.003 (0.001)	0.002 (0.000)	0.004 (0.001)	0.004 (0.001)	0.004 (0.001)	0.003 (0.001)	0.002 (0.001)	0.002 (0.001)	0.002 (0.001)	0.002 (0.002)
Fe	0.277 (0.008)	0.281 (0.011)	0.281 (0.006)	0.284 (0.007)	0.280 (0.010)	0.281 (0.003)	0.279 (0.003)	0.270 (0.007)	0.267 (0.008)	0.272 (0.003)
Mg	1.563 (0.007)	1.543 (0.019)	1.543 (0.019)	1.498 (0.011)	1.483 (0.011)	1.491 (0.007)	1.487 (0.007)	1.505 (0.014)	1.510 (0.009)	1.511 (0.019)
Ca	0.067 (0.007)	0.055 (0.014)	0.049 (0.005)	0.059 (0.005)	0.073 (0.025)	0.071 (0.002)	0.068 (0.003)	0.053 (0.004)	0.056 (0.003)	0.069 (0.004)
Na	0.003 (0.002)	0.005 (0.001)	0.003 (0.002)	0.003 (0.002)	0.003 (0.002)	0.004 (0.002)	0.003 (0.002)	0.004 (0.002)	0.003 (0.001)	0.003 (0.001)
Cat.Sum.	4.000 (0.008)	3.989 (0.012)	3.992 (0.012)	3.999 (0.002)	4.005 (0.006)	4.000 (0.006)	3.989 (0.007)	3.988 (0.007)	3.993 (0.004)	4.003 (0.005)
X <sub>Mg</sub>	0.849 (0.004)	0.846 (0.004)	0.846 (0.003)	0.841 (0.003)	0.841 (0.004)	0.842 (0.002)	0.842 (0.002)	0.848 (0.004)	0.850 (0.004)	0.848 (0.002)

X<sub>Mg</sub> = Mg/(Mg+Fe<sup>tot</sup>). Numbers in parentheses correspond to 1sigma standard deviations. Cations are calculated on the basis of 6 oxygens and all Fe = Fe<sup>2+</sup>.

Table 5. Representative compositions of olivines

Run:	GV10-83-23	GV10-83-24	GV10-83-5	GV10-83-4*	GV10-83-12	GV10-83-17	GV10-83-3	GV10-83-7	GV10-83-16*
P(GPa)	0.8	0.9	1	1	1.3	1.4	1.5	1.5	1.5
T(°C)	1100	1100	1100	1180	1150	1150	1150	1200	1230
No. An	8	4	5	10	9	7	9	15	6
SiO <sub>2</sub>	39.53 (0.13)	40.05 (0.35)	39.46 (0.35)	39.75 (0.51)	39.67 (0.57)	39.59 (0.45)	39.93 (0.42)	40.42 (0.13)	39.48 (0.13)
TiO <sub>2</sub>	0.03 (0.01)	0.03 (0.01)	0.02 (0.02)	0.03 (0.02)	0.03 (0.02)	0.03 (0.02)	0.03 (0.01)	0.03 (0.01)	0.02 (0.02)
Cr <sub>2</sub> O <sub>3</sub>	0.02 (0.02)	0.02 (0.02)	0.05 (0.03)	0.04 (0.03)	0.05 (0.03)	0.05 (0.03)	0.02 (0.02)	0.02 (0.02)	0.05 (0.03)
FeO	15.24 (0.18)	15.35 (0.22)	15.66 (0.19)	15.60 (0.26)	15.62 (0.26)	15.61 (0.24)	15.31 (0.19)	15.29 (0.12)	15.60 (0.23)
MgO	44.50 (0.04)	43.72 (0.22)	43.64 (0.46)	43.95 (0.55)	43.79 (0.41)	43.83 (0.37)	44.00 (0.41)	43.86 (0.07)	43.90 (0.32)
CaO	0.38 (0.05)	0.39 (0.05)	0.39 (0.02)	0.41 (0.04)	0.40 (0.04)	0.39 (0.03)	0.38 (0.05)	0.36 (0.01)	0.38 (0.03)
Total	99.69 (0.18)	99.57 (0.41)	99.22 (0.37)	99.77 (0.71)	99.54 (0.67)	99.49 (0.56)	99.66 (0.35)	99.98 (0.17)	99.42 (0.35)
Si	0.995 (0.003)	1.013 (0.005)	1.001 (0.012)	1.003 (0.011)	1.003 (0.012)	1.001 (0.009)	1.008 (0.010)	1.018 (0.002)	0.999 (0.004)
Ti	0.001 (0.000)	0.001 (0.000)	0.000 (0.000)	0.001 (0.000)	0.001 (0.000)	0.001 (0.000)	0.001 (0.000)	0.001 (0.000)	0.000 (0.000)
Cr	0.000 (0.000)	0.000 (0.000)	0.001 (0.001)	0.001 (0.001)	0.001 (0.000)	0.001 (0.000)	0.000 (0.000)	0.000 (0.000)	0.001 (0.001)
Fe	0.321 (0.004)	0.325 (0.005)	0.332 (0.003)	0.329 (0.006)	0.330 (0.006)	0.330 (0.005)	0.323 (0.005)	0.322 (0.003)	0.330 (0.005)
Mg	1.670 (0.002)	1.648 (0.006)	1.651 (0.012)	1.652 (0.014)	1.650 (0.013)	1.652 (0.011)	1.655 (0.012)	1.646 (0.001)	1.656 (0.007)
Ca	0.010 (0.001)	0.011 (0.001)	0.011 (0.000)	0.011 (0.001)	0.011 (0.001)	0.011 (0.001)	0.010 (0.001)	0.010 (0.000)	0.010 (0.001)
Cat.sum	2.997 (0.005)	2.997 (0.007)	2.996 (0.004)	2.996 (0.006)	2.996 (0.005)	2.996 (0.007)	2.997 (0.006)	2.996 (0.008)	2.997 (0.006)
X <sub>Mg</sub>	0.833 (0.002)	0.829 (0.003)	0.826 (0.002)	0.827 (0.004)	0.826 (0.003)	0.827 (0.003)	0.831 (0.003)	0.830 (0.001)	0.828 (0.003)

X<sub>Mg</sub> = Mg/(Mg+Fe<sup>tot</sup>). Numbers in parentheses correspond to 1sigma standard deviations. Cations are calculated on the basis of 4 oxygens and all Fe = Fe<sup>2+</sup>.

Table 6. Representative compositions of spinels

Run:	GV10-83-23	GV10-83-24	GV10-83-5	GV10-83-4*	GV10-83-12	GV10-83-17	GV10-83-3	GV10-83-7	GV10-83-16*
P(GPa)	0.8	0.9	1	1	1.3	1.4	1.5	1.5	1.5
T(°C)	1100	1100	1100	1180	1150	1150	1150	1200	1230
No. An	4	5	4	10	5	13	4	8	4
SiO <sub>2</sub>	0.14 (0.07)	0.46 (0.11)	0.27 (0.08)	0.34 (0.13)	0.13 (0.05)	0.16 (0.09)	0.26 (0.11)	0.32 (0.13)	0.27 (0.13)
TiO <sub>2</sub>	0.14 (0.07)	0.18 (0.04)	0.19 (0.06)	0.17 (0.05)	0.22 (0.06)	0.18 (0.07)	0.28 (0.08)	0.24 (0.06)	0.16 (0.02)
Al <sub>2</sub> O <sub>3</sub>	56.55 (0.38)	58.35 (0.82)	64.33 (0.07)	63.42 (0.85)	62.48 (0.77)	62.11 (0.44)	60.35 (1.15)	61.58 (0.95)	63.2 (1.07)
Cr <sub>2</sub> O <sub>3</sub>	7.23 (0.23)	5.78 (0.24)	2.24 (0.18)	2.11 (0.17)	2.16 (0.11)	1.96 (0.23)	4.96 (0.87)	3.68 (0.66)	2.76 (0.53)
FeO	17.92 (0.08)	17.90 (0.43)	15.89 (0.15)	15.05 (0.43)	17.25 (0.35)	17.68 (0.66)	17.13 (0.44)	16.79 (0.51)	15.92 (0.66)
MgO	17.92 (0.11)	17.38 (0.42)	17.30 (0.22)	17.78 (0.55)	17.34 (0.49)	17.24 (0.55)	16.93 (0.86)	17.16 (0.72)	16.79 (0.37)
Total	99.89 (0.08)	100.05 (0.70)	100.20 (0.16)	98.87 (0.32)	99.58 (0.26)	99.33 (0.35)	99.91 (0.67)	99.77 (0.59)	99.1 (0.51)
Si	0.004 (0.002)	0.012 (0.003)	0.007 (0.002)	0.009 (0.002)	0.003 (0.001)	0.004 (0.002)	0.007 (0.002)	0.008 (0.002)	0.007 (0.002)
Ti	0.003 (0.001)	0.003 (0.001)	0.004 (0.001)	0.003 (0.001)	0.004 (0.001)	0.004 (0.001)	0.005 (0.001)	0.005 (0.001)	0.003 (0.001)
Al	1.749 (0.010)	1.797 (0.010)	1.943 (0.002)	1.934 (0.007)	1.906 (0.005)	1.901 (0.007)	1.854 (0.011)	1.883 (0.009)	1.936 (0.011)
Cr	0.150 (0.005)	0.119 (0.006)	0.045 (0.004)	0.043 (0.006)	0.044 (0.004)	0.040 (0.006)	0.102 (0.009)	0.076 (0.008)	0.057 (0.006)
Fe	0.393 (0.002)	0.391 (0.012)	0.340 (0.003)	0.326 (0.008)	0.373 (0.006)	0.384 (0.008)	0.373 (0.007)	0.364 (0.008)	0.346 (0.007)
Mg	0.701 (0.004)	0.677 (0.014)	0.661 (0.008)	0.686 (0.009)	0.669 (0.007)	0.667 (0.009)	0.658 (0.011)	0.664 (0.009)	0.651 (0.006)
X <sub>Mg</sub>	0.641 (0.015)	0.634 (0.005)	0.660 (0.006)	0.678 (0.010)	0.642 (0.004)	0.635 (0.011)	0.638 (0.013)	0.646 (0.008)	0.653 (0.010)
X <sub>Cr</sub>	0.079 (0.004)	0.062 (0.007)	0.023 (0.008)	0.022 (0.009)	0.023 (0.004)	0.021 (0.008)	0.052 (0.011)	0.039 (0.009)	0.028 (0.009)

X<sub>Cr</sub> = Cr/(Cr + Al); X<sub>Mg</sub> = Mg/(Mg+Fe<sup>tot</sup>). Numbers in parentheses are 1sigma standard deviations. Cations are calculated on the basis of 4 oxygens and all Fe = Fe<sup>2+</sup>.

Table 7. Representative compositions of plagioclases and garnets

Run:	GV10-83-25	GV10-83-23	GV10-83-24		GV10-83-3	GV10-83-7	GV10-83-16*
P(GPa)	0.7	0.8	0.9	P(GPa)	1.5	1.5	1.5
T(°C)	1100	1100	1100	T(°C)	1150	1200	1230
No. An	6	5	6	No. An	5	13	9
SiO <sub>2</sub>	49.63 (0.87)	52.54 (0.40)	53.48 (0.07)	SiO <sub>2</sub>	43.14 (0.22)	43.22 (0.26)	43.24 (0.25)
TiO <sub>2</sub>	0.04 (0.02)	0.05 (0.01)	0.05 (0.01)	TiO <sub>2</sub>	0.22 (0.05)	0.22 (0.04)	0.23 (0.04)
Al <sub>2</sub> O <sub>3</sub>	32.13 (0.57)	29.43 (0.38)	29.35 (0.74)	Al <sub>2</sub> O <sub>3</sub>	22.34 (0.24)	21.83 (0.82)	21.53 (1.08)
FeO	0.18 (0.07)	0.06 (0.06)	0.11 (0.02)	Cr <sub>2</sub> O <sub>3</sub>	0.16 (0.05)	0.16 (0.04)	0.18 (0.04)
MgO	0.16 (0.09)	0.15 (0.07)	0.16 (0.05)	FeO	10.26 (0.44)	10.33 (1.22)	10.52 (1.47)
CaO	14.31 (0.32)	14.49 (0.34)	12.70 (0.33)	MgO	18.35 (0.61)	18.29 (0.83)	18.27 (0.95)
Na <sub>2</sub> O	3.44 (0.18)	3.79 (0.18)	4.43 (0.13)	CaO	6.32 (0.34)	6.71 (0.76)	6.89 (0.87)
K <sub>2</sub> O	0.08 (0.07)	0.03 (0.01)	0.04 (0.01)	Na <sub>2</sub> O	0.07 (0.03)	0.06 (0.03)	0.04 (0.03)
Total	99.95 (0.33)	100.59 (0.26)	100.28 (0.82)	Total	100.93 (0.51)	101.15 (0.69)	100.97 (0.64)
Si	2.257 (0.034)	2.378 (0.016)	2.417 (0.021)	Si	3.064 (0.008)	3.044 (0.091)	3.077 (0.020)
Ti	0.001 (0.000)	0.002 (0.000)	0.002 (0.000)	Ti	0.012 (0.002)	0.012 (0.002)	0.012 (0.002)
Al	1.722 (0.034)	1.570 (0.020)	1.563 (0.027)	Al	1.870 (0.028)	1.827 (0.072)	1.806 (0.093)
Fe	0.006 (0.001)	0.002 (0.002)	0.004 (0.001)	Cr	0.009 (0.003)	0.010 (0.002)	0.010 (0.002)
Mg	0.011 (0.005)	0.010 (0.004)	0.011 (0.003)	Fe	0.607 (0.023)	0.591 (0.074)	0.584 (0.088)
Ca	0.697 (0.016)	0.702 (0.016)	0.615 (0.014)	Mg	1.942 (0.061)	1.920 (0.084)	1.937 (0.092)
Na	0.303 (0.015)	0.333 (0.016)	0.388 (0.013)	Ca	0.481 (0.027)	0.506 (0.063)	0.525 (0.068)
K	0.001 (0.001)	0.000 (0.000)	0.000 (0.000)	Na	0.009 (0.005)	0.008 (0.003)	0.006 (0.004)
Cat.Sum.	4.998 (0.009)	4.998 (0.011)	5.000 (0.013)	Cat.Sum.	7.994 (0.008)	7.969 (0.009)	7.957 (0.012)
Ca+Na	1.000 (0.021)	1.035 (0.022)	1.003 (0.018)	X <sub>Mg</sub>	0.760 (0.008)	0.754 (0.012)	0.756 (0.034)
An	0.696 (0.015)	0.679 (0.016)	0.613 (0.013)				

An = Ca/(Ca + Na); X<sub>Mg</sub> = Mg/(Mg+Fe<sup>tot</sup>). Numbers in parentheses correspond to 1sigma standard deviations. Cations are calculated on the basis of 8 and 6 oxygens for plagioclase and garnet, respectively. All Fe = Fe<sup>2+</sup>.

Table 8. Phase proportions (wt%) in experiments calculated by weighted mass balance

Run	P(GPa)	T(°C)	cpx	opx	ol	sp <sub>g</sub>	plg <sub>g</sub>	gnt <sub>g</sub>	R2*
GV10-83-25	0.7	1100	60.0(3.1)	12.6(3.7)	11.9(2.6)	1.7(0.9)	13.7(2.1)	0	0.389
GV10-83-23	0.8	1100	59.0(1.7)	14.9(3.2)	11.4(2.5)	3.2(0.6)	11.8(1.8)	0	0.256
GV10-83-24	0.9	1100	62.4(1.6)	16.2(3.1)	9.1(2.6)	3.8(0.8)	8.7(1.9)	0	0.287
GV10-83-5	1.0	1100	76.2(4.5)	14.4(2.8)	4.7(1.2)	4.6(1.1)	0	0	0.142
GV10-83-4*	1.0	1180	74.4(2.7)	16.1(5.1)	5.2(2.9)	4.5(1.3)	0	0	0.213
GV10-83-12	1.3	1150	79.4(1.6)	11.8(3.2)	4.9(1.9)	4.1(0.6)	0	0	0.095
GV10-83-17	1.4	1150	77.4(3.9)	13.7(6.4)	4.1(3.2)	4.7(1.1)	0	0	0.263
GV10-83-3	1.5	1150	71.1(2.7)	10.1(3.2)	5.8(2.3)	2.4(2.1)	0	10.5(3.7)	0.147
GV10-83-7	1.5	1200	75.6(3.2)	7.6(2.7)	6.1(3.2)	2.1(0.9)	0	8.2(2.5)	0.244
GV10-83-16*	1.5	1230	78.1(4.1)	6.7(5.3)	6.3(2.1)	3.1(1.9)	0	5.2(4.6)	0.342

(\*) Sum of the squares of residuals for all elements calculated as the sum of the squares of the difference between model and calculated composition.  
cpx, clinopyroxene; opx, orthopyroxene, ol, olivine; sp<sub>g</sub>, spinel; plg<sub>g</sub>, plagioclase; gnt<sub>g</sub>, garnet.  
Numbers in parentheses are propagated errors from Monte Carlo simulations.